A review of recent *z*-pinch research at Maxwell Physics International

P.L. COLEMAN,[1] B.H. FAILOR, J.S. LEVINE, J.C. RIORDAN,
Y. SONG,[2] H. SZE, AND E.M. WAISMAN[1]

Titan Pulsed Sciences (formerly Maxwell Physics International), 2700 Merced Street, San Leandro, CA 94577

1. INTRODUCTION AND SUMMARY

During the last few years, we have concentrated on developing plasma radiation sources (PRS) for the longer current rise time (up to 300 ns) of the direct-drive Decade Quad (DQ; Price *et al.*, 1999). In particular, we have developed an argon gas-puff PRS that produces a high quality pinch with an ~200-ns implosion time, twice the implosion time of typical *z* pinches. We have shown that large-diameter, solid-fill (i.e., the gas density is a smooth function of the radial distance rather than a discrete shell) gas puffs can achieve adequate heating and stability for long-implosion *z* pinches with good *K*-shell yield.

To produce high X-ray yields, a ~200 ns *z* pinch must reach a temperature and density in the final plasma comparable to a conventional ≤100-ns implosion. This requires that a long-implosion-time *z* pinch start from larger initial radius and still achieve high compression, as described in Section 2. The hydromagnetic Rayleigh–Taylor instability will disrupt the implosion of large-diameter, hollow shells, limiting the temperature and density of the radiating mass. The data presented here and elsewhere show that the instability is effectively mitigated for large loads by continuous mass accretion during the "snowplow" of a filled-in initial density profile.

In our initial experiments, we developed a solid-fill argon gas puff with a 7-cm diameter for high X-ray yields with ~200-ns implosions. Section 3 describes those experiments. On Double-EAGLE (Frazier *et al.*, 1983), we demonstrated ≥13 kJ *K*-shell X-ray yield with a 4.0-MA peak current and a 190-ns implosion time. Long-implosion time

tests were also performed on DM2 (Sincerny *et al.*, 1995) at 2.3-MA and Saturn (Bloomquist *et al.*, 1987) at 6.5-MA. Our data confirm that the long-implosion yield has an I^4 current scaling up to 4 MA as observed for ~100 ns PRS.

We next developed a large radius double shell ("shell-on-shell") gas puff. It performs as well as the 7-cm uniform fill load. The nozzle's dual plenum feature permits some very useful diagnostics that shed light on critical details of the implosion process. Very recently, we successfully used this nozzle for ~100 ns argon implosions on the Z generator (Spielman *et al.*, 1998), producing over 270 kJ of *K*-shell yield with 15 MA (Sze *et al.*, 2001). See Section 4 for details.

With the objective of understanding the possibilities for long implosion times in general, we have also observed good X-ray emission from large-diameter wire array loads. Such loads may be required for mixed-element, higher-fidelity broad-spectrum *z*-pinches. We performed long-implosion tests of aluminum wire arrays with 4-cm diameter on DM2, Double-EAGLE, and Saturn. The respective *K*-shell yields were 4 kJ, >18 kJ, and >60 kJ. A wire number scan in the Double-Eagle long-pulse mode confirmed the pulse-sharpening effects of higher wire counts that have previously been observed for short implosion times. However, *K*-shell yield does not benefit from increased wire number. We also tested molybdenum wire arrays with a 2.5-cm diameter in the Double-Eagle short-pulse mode (4.5 MA, 100 ns). The *L*-shell yield (with a mean photon energy of 2.6 keV) was <3 kJ, significantly lower than the >20 kJ argon *K*-shell yield at similar current and implosion time.

Section 5 summarizes all of the above results for long-implosion-time loads and compares their performance with that of "short"-implosion-time loads. We identify empirical trends and discuss some of the physics behind the trends.

Detailed measurements of local conditions in the final pinched plasma were performed to understand the similarities and differences between long- and short-implosion PRS.

Address correspondence and reprint requests to: P.L. Coleman, Alameda Applied Sciences Corporation, 2235 Polvorosa Ave., #230, San Leandro, CA 94577, USA. E-mail: plcoleman@mailaps.org

[1]Now at Alameda Applied Sciences Corporation, 2235 Polvorosa Ave., #230, San Leandro, CA 94577, USA.

[2]Now at Department of Physics, University of California, Irvine, Irvine, CA 92697, USA.

Section 6 presents analyses of spectra using a chlorine dopant to obtain temperature and density measurements for the Double-Eagle argon experiments. Axially resolved spectra show more intense emission from regions that are initially filled in, and that higher density leads to better thermalization of the ion energy. Average plasma conditions inferred from chlorine are consistent with the measured argon yields.

Finally, Section 7 covers some advances in diagnostics and an improved preionizer for more uniform initiation of current flow on a gas puff.

2. BASIC SCALING CONSIDERATIONS FOR LONG-IMPLOSION-TIME *Z* PINCHES

"Cold" X rays (1–5 keV) have been produced in many laboratories using *z*-pinch plasma radiation sources (Pereira & Davis, 1988; Spielman *et al.*, 1989; Deeney *et al.*, 1994). In a typical *z* pinch, an annular "shell" gas puff or cylindrical array of wires is accelerated radially inward by the $\mathbf{J} \times \mathbf{B}$ interaction of the pinch current and its self-generated magnetic field. The imploding mass ultimately stagnates on the pinch axis, creating a hot, dense plasma that converts the kinetic energy of the implosion to radiation. Experiment and theory have shown that the X-ray yield increases as the imploded mass increases. For low masses, the yield varies as the product of electron and ion densities, that is, as the square of the mass. Simple dynamic arguments (see below) show that for fixed initial radius and a fixed implosion time, the imploded mass varies as the square of the peak current. Hence, for a fixed implosion velocity (roughly load radius divided by implosion time), the yield should scale as the fourth power of the peak current, I^4. This is termed the "inefficient" regime. As the radiated yield becomes comparable to the available kinetic energy, energy conservation limits the yield. Then we expect the yield to increase as the mass or as I^2; this is called the "efficient" regime (Whitney *et al.*, 1994; Thornhill *et al.*, 1996). For *K*-shell emission, the current at which yield becomes "efficient" increases with at least the cube of the atomic number of the radiating plasma; for example, ~5 MA for argon ($Z = 18$) and ~10 MA for titanium ($Z = 22$); see Whitney *et al.* (1990) and Mosher *et al.* (1998).

Until recently, most PRSs have operated with implosion times of 100 ns or less, requiring megavolt pulsed-power generators to drive the required current into the inductive PRS load. Higher-current X-ray simulators envisioned to produce higher X-ray yields at higher photon energies must then operate at higher voltages. Unfortunately, the higher voltage operation requires additional volume and inductance, thereby limiting the electrical power that can be coupled through the dielectric-vacuum interface from the pulsed power generator to the load. During the past decade, much effort has been devoted to the development of inductive-store, plasma-opening-switch (IS/POS) systems that can perform power multiplication in vacuum. The development of a high-current, fast-opening switch has proven to be a

technological challenge with some success to date on the ACE 4 (Rix *et al.*, 1993) generator.

A "long"-implosion-time (>150 ns) PRS provides an alternative approach that can mitigate the pulse-power risk in either higher voltage conventional machines or IS/POS designs. The longer implosion time allows the current to ramp up more slowly, thereby reducing the voltage and power requirements on the generator. In effect, the PRS provides additional pulse compression in vacuum as the electromagnetic energy from the generator is converted into kinetic energy in the imploding *z*-pinch. The key risk in this approach is whether the radiation efficiency of the short (≤100-ns) implosion can be maintained at significantly longer implosion times. Our objective has been to quantify the efficiency of PRSs as a function of implosion time.

To achieve good *K*-shell X-ray emission from a PRS, it is necessary to heat the plasma to a temperature of at least 30% of the He-α line energy, or $T_e > 1$ keV for argon. This requires that the kinetic energy of an imploding atom exceed a minimum energy E_{min} equal to the sum of the outer shell ionization energies plus the electron and ion thermal energies ($E_{min} = 40$ keV for argon). This requirement is expressed by the condition $\eta > 1$, where η is the kinetic energy per atom divided by E_{min} (Whitney, 1990). Since the implosion velocity scales as the initial radius divided by implosion time, the initial radius must increase in proportion to the implosion time to maintain the same velocity and η.

It is straightforward to show that for a shell of mass/length m at initial radius r_0, the implosion time t_{imp} and peak current I_{pk} are related by the general relation

$$m = k(I_{pk} t_{imp}/r_0)^2$$

where the constant, k, depends on the shape of the radial mass distribution of the imploding mass (a shell or solid fill, etc.) and on the shape of the current's rise to its peak value. For example, with mass in micrograms per centimeter, current in megamperes, time in nanoseconds, and radius in centimeters, a linear current ramp driving an ideal shell has a value for k of 0.0012. For other mass distributions, use the mean radius as defined below for r_0.

Assuming the short and long implosions have the same ratio of initial radius to implosion time, then the mass/length scales as the peak current squared independent of implosion time. Thus in the "efficient" regime, both long- and short-implosion PRS with the same peak currents should produce the same X-ray yield, provided they can achieve the same compression ratio (ratio of initial to final radii) required to maintain η.

In the noneffcient (I^4 scaling) regime, the PRS plasma must also achieve high density to radiate a significant X-ray yield because the X-ray power is proportional to the product of electron and ion densities (n_e and n_i). Assuming that the radiating volume and pulse width respectively scale as r_f^2 and r_f, where r_f is the final compressed radius of the pinch, the yield then scales as mass-squared (Thornhill *et al.*, 1996):

$$Y \propto n_e n_i r_f^3 \propto m^2/r_f.$$

But we see that the yield also scales inversely with r_f, so the long-implosion PRS must pinch to the same final radius to maintain the X-ray yield. Since the long implosion starts at a larger initial radius, it requires a higher compression ratio to achieve the same final radius and density achieved in the short-implosion PRS.

Imploding z pinches are susceptible to the hydromagnetic Rayleigh–Taylor (R-T) instability, which can limit the density and temperature achieved in a PRS. Two-dimensional magneto-hydrodynamic simulations predict large-scale "bubble and spike" structures that disrupt the implosion of thin shells, especially for large initial diameters (Petersen *et al.*, 1996, 1997). Nevertheless, other theoretical studies have shown that the R-T instability is mitigated for filled-in density profiles, where the continuous mass accretion provides "snowplow stabilization" (Golberg & Velikovich, 1993; Roderick *et al.*, 1998).

We have experimentally examined long-implosion PRS using large-diameter gas puffs with both shell and solid-fill density profiles. For a filled gas puff, the implosion energy includes not only kinetic energy but also shock heating associated with the snowplow; thus η is generalized to a quantity η^* defined as the total $\mathbf{J} \times \mathbf{B}$ work per atom divided by E_{min}. If we define a mass-weighted-mean initial radius as the second moment of the radial density profile $\rho(r)$, then the initial outer radius of a uniform fill distribution (constant density) must be 41% larger than that of a thin shell to have the same mean radius. If the compression ratio is defined as the ratio of the mean initial radius to the final pinch radius, then shell and uniform-fill loads with equal compression ratios will reach the same final density and η^* (based on a snowplow calculation).

On the basis of these concepts, we come to the following expectations. Assume that a given pulsed power generator like Double-EAGLE can reach the same peak current ($\sim$4 MA) independent of current rise time. Assume that compression ratio (mean initial radius to final pinch radius) is fixed. Then at a fixed implosion time, ideal shell and corresponding uniform fill mass distributions will give similar yields if instabilities are not serious. As implosion time is increased and thus initial radius is increased, the final radius will also increase and yield will decrease roughly inversely with implosion time for "inefficient" radiators like argon.

With the objective of understanding how to build a gas puff load that can deliver 40 kJ of argon K-shell radiation with a 300-ns implosion time on DQ, we conducted experiments to test the expectations noted above. In brief, we find that a nominal gas "shell" load always performs worse than the corresponding uniform fill load (Riordan *et al.*, 1998). This result confirms results seen in earlier experiments on ACE 4 (Coleman *et al.*, 1997) and Saturn (Sanford *et al.*, 1996a). The implication is that (1) instabilities do seriously disrupt the shell implosions and (2) snowplow stabilization is effective for the uniform fill loads.

A second key observation from our tests is that there is a yield penalty as implosion time increases in the inefficient regime. The exact dependence is not well established but to zeroth order the yield varies inversely with implosion time for currents up to about 4 MA. The implication is that the compression ratio of the pinch is roughly fixed. Although simple models exist to explain this result, the models cannot explain why some key pinch parameters, such as K-shell pulse width, do not seem to be well correlated with implosion time. In particular, long implosion times do not always imply wide pulse width, which should scale with the final pinch radius. In spite of these complications, our results (Section 3) show that we know enough to design a gas flow that should reach the 40 kJ objective on DQ with a 300-ns current risetime.

3. DEVELOPMENT OF UNIFORM-FILL GAS LOADS FOR LONG-IMPLOSION-TIME Z PINCHES

We started our research effort from the "tradition" of using nominal "shell" loads in 100-ns implosions. The Double-EAGLE 2.5-cm-diameter argon gas puff was the basis for that tradition. Our challenge was to demonstrate good quality 200-ns implosions that were not hopelessly disrupted by instabilities. We began with a comparison of two loads appropriate for 200-ns implosion times: a 5-cm-diameter "shell" and the corresponding 7-cm-diameter (40% larger) uniform fill. In tests first on DM2 and then on Double-EAGLE, we showed that the uniform fill could work well and that it was always superior (by >40% in yield and >100% in power) to the shell load. Table 1 compares yield and peak K-shell power data from those experiments as well as comparable data from ACE 4.

In Section 5 we review these data empirically to see that they scale with current as expected and to demonstrate how they correlate with short implosion time data.

In this section we also discuss a limited number of tests with a 10-cm-diameter uniform-fill nozzle; those results were encouraging, showing that such large loads are not seriously disrupted by instabilities. Hence all of our data imply that a large-radius uniform-fill load is a practical approach to achieving the desired 40-kJ K-shell yield on DQ. We now describe some of our test results for long-implosion-time loads. Most of our efforts used Double-EAGLE and those results are presented in Section 3.1. DM2 and Saturn results will not be discussed in detail.

3.1. Double-EAGLE argon PRS experiments

We used several test series to optimize the K-shell X-ray yield from an argon gas puff with a long implosion time. Our key objective was to understand significant physics differences between long- and short-implosion PRS. Double-EAGLE was selected as the test bed because it can deliver high current (up to 4 MA) with a rise time adjustable from

Table 1. *Comparison of shell and uniform-fill long-pulse argon results on 3 machines.*

Machine	Current (MA)	Implosion time (ns)	7-cm uniform fill		5-cm shell	
			K-power (TW)	K-yield (kJ)	K-power (TW)	K-yield (kJ)
DM2	2.3	300	0.08	1.7	0.04	1.2
ACE 4	2.9	200	0.7	3.7	0.2	1.9
Double-EAGLE	3.6	180	0.8	13	0.3	6.8

100 to 300 ns. Using a 7-cm-diameter solid-fill gas puff, we achieved a >13-kJ X-ray yield and a <16 ns pulse width (FWHM) with a 180-ns implosion time. Spectral diagnostics indicate that the density in the radiating core decreased by a factor >2 for the longer implosion time (compared to 100-ns implosions), while the temperature showed no significant change (see Section 6 for details). We also confirmed that the long-implosion yield scaled as I^4 for currents up to at least 4.0 MA.

3.1.1. Double-EAGLE long-pulse mode

For a given pulse-power generator, the X-ray output from a PRS is typically optimized when the implosion time is nearly equal to the rise time of the current pulse into a nonimploding load. The conventional argon PRS on Double-EAGLE, for example, gives maximum X-ray yield at a 100-ns implosion time that is equal to the rise time of the short-circuit current. Thus, to investigate an optimized 200-ns implosion PRS, we needed a test bed with a 200-ns current rise time. Fortunately, the design of the Double-EAGLE pulse-forming line (PFL) provides sufficient flexibility to extend the current rise time to 200 ns with no decrease in peak current. This long-pulse operating mode is achieved by completely closing the water switch gaps downstream from the PFL and by reducing the water switch gaps upstream of the PFL from 13 cm to 4 cm. (Operation at even longer current pulses is possible on Double-EAGLE, but was not pursued extensively for these experiments.) Current waveforms upstream and near the load (Fig. 1) are in excellent agreement, indicating full current coupling through the MITLs and convolute, even in the long-pulse mode; see Figure 2. Furthermore, the current dip caused by the back electromotive force ($I * dL/dt$) of the imploding pinch is clearly visible on all waveforms, indicating that the load is well-coupled to the generator.

For the long-implosion PRS, we wanted to produce a z-pinch plasma with the same implosion velocity as that of the standard Double-EAGLE argon PRS, which uses a 2.5-cm-diameter shell with a 100-ns implosion time. Thus, we chose a 5-cm mean diameter to give the same final velocity for the 200-ns implosion. However, it is important to note that achieving the same final density would require reaching the same final radius, which is a factor of 2 higher compression than achieved with the 100-ns implosion. In comparing

short- and long-implosion PRS, we also wanted to investigate a "solid-fill" gas puff that had demonstrated improved X-ray output in previous experiments (Coleman *et al.*, 1997). Thus, we selected a 7-cm initial outer diameter for the solid fill nozzle to provide an effective diameter equal to a 5-cm-diameter shell.

We made use of three different gas puffs; see Figure 3. The long-implosion nozzles were designed using a viscous, transient gas-dynamic code (Chapman, 1980). The solid-fill nozzle is actually a wide annulus with a central stub that protects the puff valve from debris. The solid-fill nozzle had a 90%-open mesh attached to its exit plane to define the electrical cathode plane. All three loads had the same 3.8-cm pinch length, which was defined by an array of wires attached to 12-current return posts.

Because PRS z pinches typically operate on the rising portion of the transient gas flow, the density will always be higher near the nozzle (cathode) than at the anode end. In addition, radial expansion causes a broadening of the radial profile as one moves downstream. Initial density measurements (Weber *et al.*, 1997; Stephanakis *et al.*, 1998) for plenum pressures and flow times similar to those used on Double-EAGLE are shown in Figure 4 for the 5-cm-
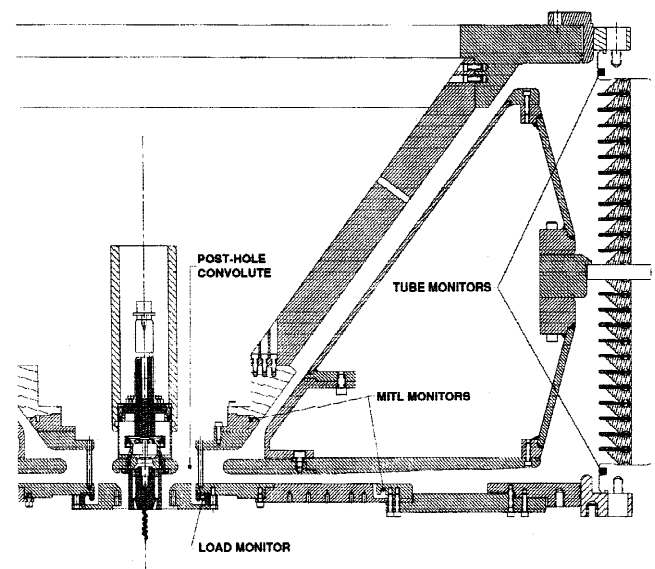
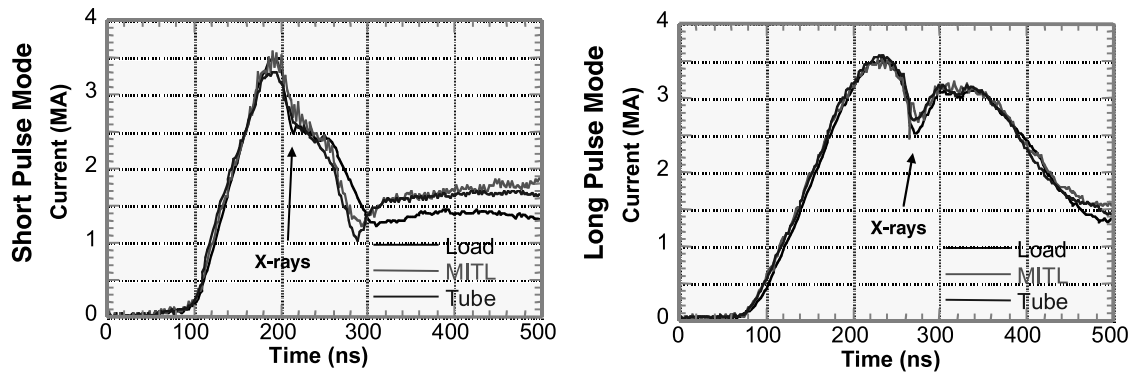**Fig. 1.** Location of Double-EAGLE current monitors.

Fig. 2. Current monitors show excellent power coupling through the convolute to the load in both "short" and "long" pulse modes.

diameter shell and the 7-cm-diameter solid fill. Shell profiles are indeed hollow near the nozzle, but become partially filled in at the midpoint, and nearly solid-fill at the anode end; the mass/length decreases by 39% from cathode to anode (i.e., $z = 2$ mm to $z = 4$ cm). As we show below, the 5-cm-diameter "shell" nozzle radiates best away from the nozzle, where, in fact, the gas density distribution is more uniform than shell-like. This behavior of gas flow and pinch performance is even true for the 2.5-cm-diameter "shell" nozzle that is used for short (100-ns) operation. The solid-fill profiles show much less change (in gas flow and emission) from cathode to anode and the mass/length decreases by only 16% over the same distance. Such data on the mass distributions, derived from precision interferometry at the Naval Research Lab, have been critical to understanding our experimental results and guiding further developments.

Ultraviolet preionization was used on virtually all of our experiments. The long-pulse experiments used a robust, circular flashboard that provided >1% ionization at the periphery with excellent azimuthal uniformity (Section 7). The short pulse experiments used the standard Double-EAGLE preionizer consisting of an opposing pair of flat flashboards with much less intensity and uniformity.

3.1.2. Optimization of shell and solid-fill loads

At the standard 60-kV Marx charge, Double-EAGLE delivered ~3.5 MA to both long-implosion loads, as shown in Figure 5. Implosion times were typically near 200 ns; here the implosion time is defined as the difference between the baseline intercepts of linear fits to the leading edge of the X-ray power and load current waveforms.

The solid-fill gas puff produced argon K-shell X-ray yields that were ~50% higher than those of the shell gas puff. The primary yield diagnostic for all of our experiments consisted of a set of three tantalum foil calorimeters (7.3-μm thick) all filtered by 17-μm-thick Kapton, 4-μm-thick Kimfol, and 1.8-μm-thick aluminum; a filter transmission of 55% was calculated from a typical measured spectrum. The yield, Figure 6, was not a strong function of implosion time for the solid-fill PRS. For the shell, the optimum was somewhat better defined at about 190 ns.

The solid-fill PRS produced an X-ray pulse that was typically 30% narrower than that of the shell load. For near-optimum shots, the zipper effect accounts for one-third of the pulse width, while the remaining two-thirds (about 10 ns) is the intrinsic width that could be achieved if zippering were completely eliminated. The higher X-ray yield and
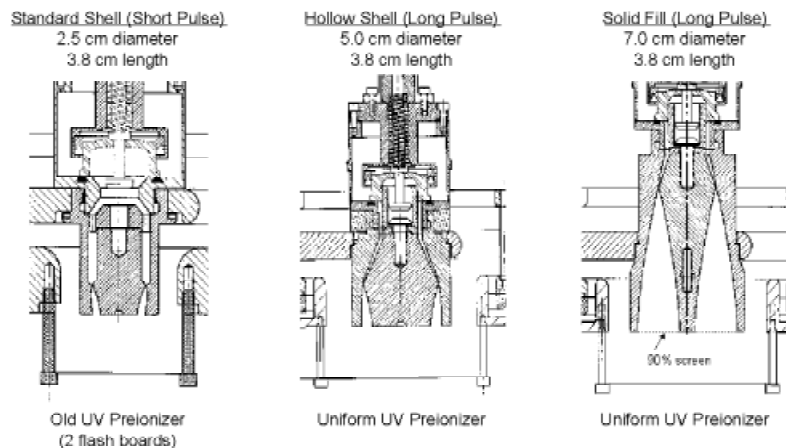

Fig. 3. Hollow shell and solid fill gas puffs load configurations.

5-cm Shell

7-cm Solid Fill

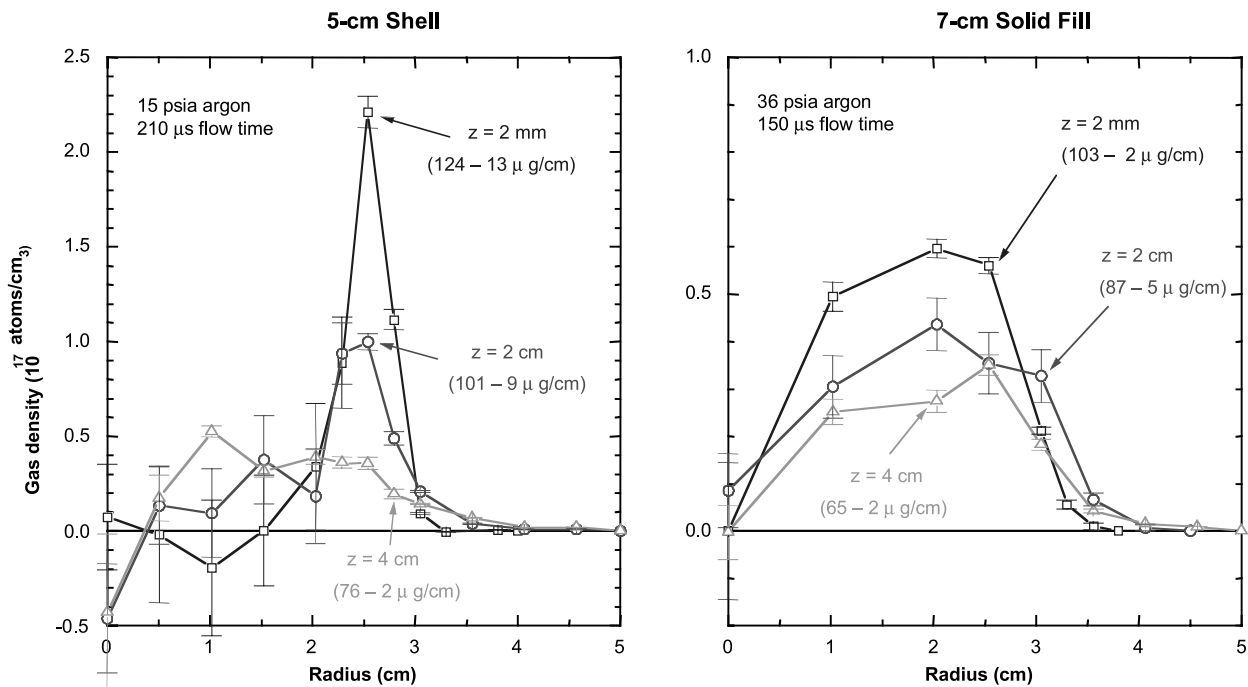**Fig. 4.** Initial density profiles for shell and solid-fill gas puffs.

narrower X-ray pulse for the solid-fill PRS produced an X-ray power that was ~100% higher than that of the shell.

Time integrated X-ray images (Fig. 7) show significant differences between solid-fill and shell PRSs. The solid-fill PRS gave fairly uniform X-ray emission over most of the pinch length. The optimized shell PRS, however, gave stronger emission near the anode (where the shell is filled in) and only weak emission near the cathode or nozzle (where the shell is hollow). This is probably due to instability in the hollow shell. (The absorption features at the anode end and also in the center of the images are artifacts of the anode wires, which partially obscure the diagnostic lines of sight

tilted at 66° to the pinch axis. Each image is color scaled for intensity independently; comparisons should not be made between images based on color.)

Thus, the solid-fill PRS is clearly superior to the shell PRS because it produces 50% higher X-ray yield and 100% higher X-ray power. In the solid fill PRS, the initial conditions vary gradually enough from cathode to anode that one can optimize emission along the entire pinch length by simultaneously adjusting plenum pressure and flow time. The shell PRS, on the other hand, is difficult to optimize along its entire length because the initial conditions change markedly from cathode to anode.
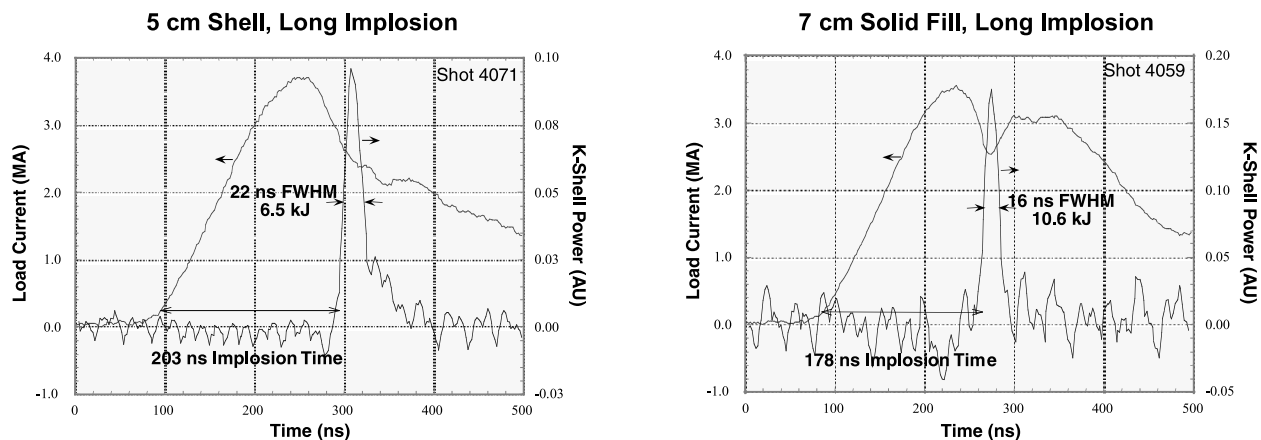
5 cm Shell, Long Implosion

7 cm Solid Fill, Long Implosion

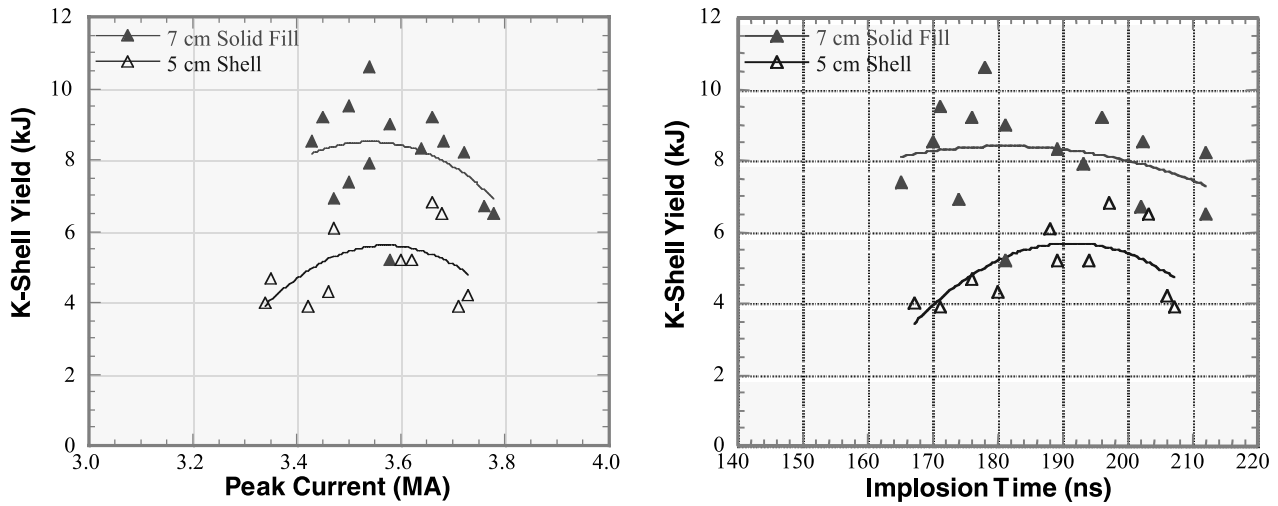**Fig. 5.** Current and X-ray power waveforms for typical shell and solid-fill PRSs.

Fig. 6. *K*-shell X-ray yield as a function of peak current and implosion time.

3.1.3. Comparison of short-and long-implosion PRS

It is instructive to compare the X-ray performance and plasma conditions of the optimized 7-cm-diameter solid-fill PRS for long implosions to those of the 2.5-cm-diameter shell load, which is used as the standard short-implosion argon PRS on Double-EAGLE (Deeney *et al.*, 1994). Figure 8 presents typical load current and X-ray power waveforms for the short- and long-implosion PRS. Note that the load currents have similar peaks and shapes, with the exception of a factor of ∼2 in rise time. Both X-ray power waveforms show a single, clean pulse, but the pulse width is a factor of 1.5 to 2 larger for the long-implosion PRS. Table 2 presents a comparison of key performance parameters for typical short- and long-implosion PRS.

Additional X-ray measurements were performed to diagnose the plasma conditions that underlie the PRS X-ray performance. *K*-shell X-ray images, for example, provide critical information on the size of the X-ray-radiating core. From Figure 7, we have determined the radiating diameter (best-fit Gaussian FWHM) as a function of position along the pinch axis. The results (Figure 9) show that the long-implosion PRS is consistently wider than the short-implosion
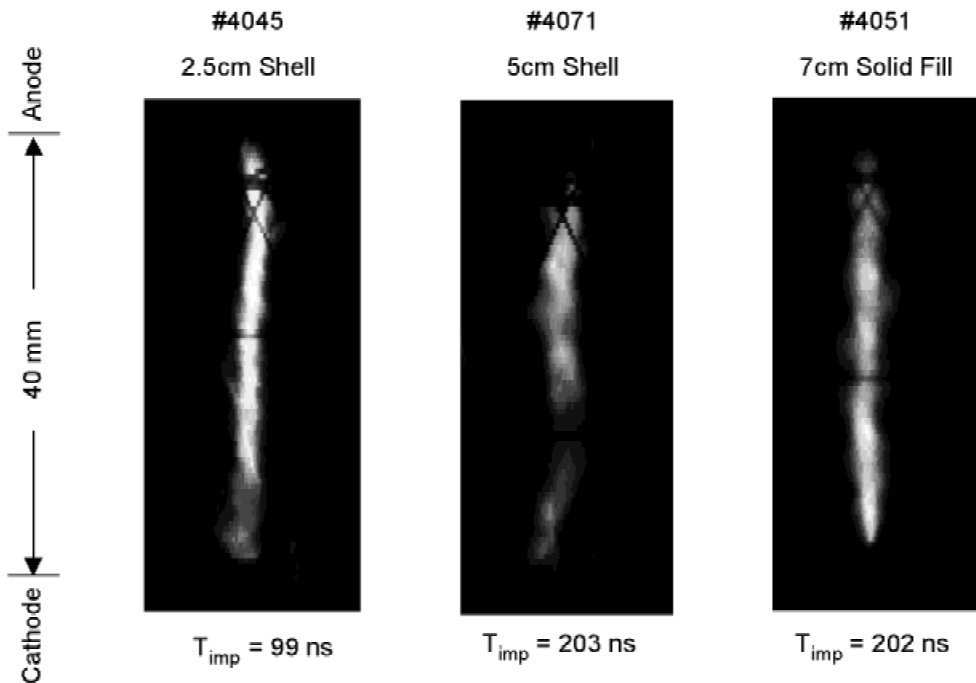

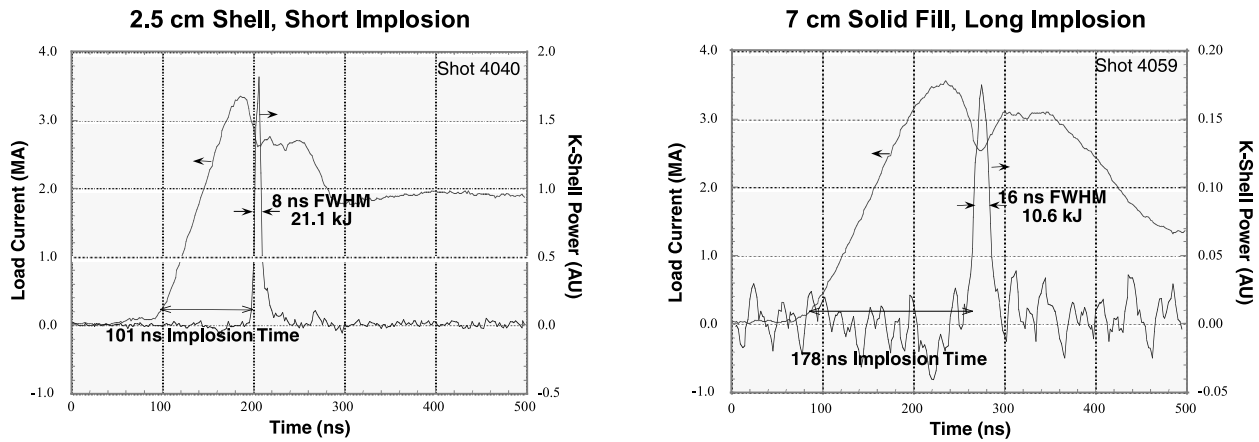**Fig. 7.** Time-integrated *K*-shell X-ray images of short- and long-implosion PRSs.

Fig. 8. Current and X-ray power waveforms for short- and long-implosion PRSs.

PRS; the only exception is the region near the cathode (nozzle), where the hollow shell pinches poorly. Taking an intensity-weighted axial average, we find that the 2.1-mm average radiating diameter of the long-implosion PRS is about 30% larger than the 1.6-mm average diameter for the short-implosion PRS.

K-shell spectra were measured using time-integrated and time-resolved spectrometers that are described in detail in Section 6. Figure 10 compares the time- and spatially integrated spectra for the short- and long-implosion PRS. The He-α resonance and intercombination (IC) lines near 3.1 keV dominate both spectra, but the Ly-α line has a higher relative intensity for the short-implosion PRS. Faint chlorine *K*-lines from a 2% CCl_2F_2 dopant can also be seen near 2.8 keV. Figure 11 shows axially resolved data for the argon He line emission (α + IC) and the ratio of the Ly-α to helium lines. These data confirm that the long-implosion, solid-fill PRS radiates uniformly over most of the nominal pinch length. The short-implosion, shell PRS radiates more intensely near the anode (where it is filled in) and weakly near the cathode (where it is hollow).

Plasma density and temperature in the *K*-shell radiating core were determined from time-integrated, axially resolved *K*-shell spectra of both argon and chlorine. In the case of argon, the temperature was determined primarily from the

Ly-α/(He-α+IC) line ratio, while the density was determined primarily from the *K*-shell brightness (Apruzese *et al.*, 1997). For the chlorine case, the electron temperature was determined from the He-α/jkl satellite line ratio, the ion temperature was determined from the IC line width, and the density was determined from the He-α/IC line ratio (Section 6). In all cases, we obtained axially-resolved profiles of temperature and density, which were then averaged to give the results displayed in Table 3.

The core temperature measurements generally show little difference between long and short implosions. This result validates our load design approach of scaling initial radius with implosion time to maintain temperature and η^*. However, the electron temperature estimates from argon are consistently higher than from chlorine. Because the argon He-α line is optically thick, we believe that absorption in the cooler halo (which is neglected in the model) causes an overestimate of core electron temperature using argon data; this effect will be more pronounced for the higher-density, short-implosion PRS.

Table 2. *Comparison of typical PRS performance with short- and long-implosion PRSs.*

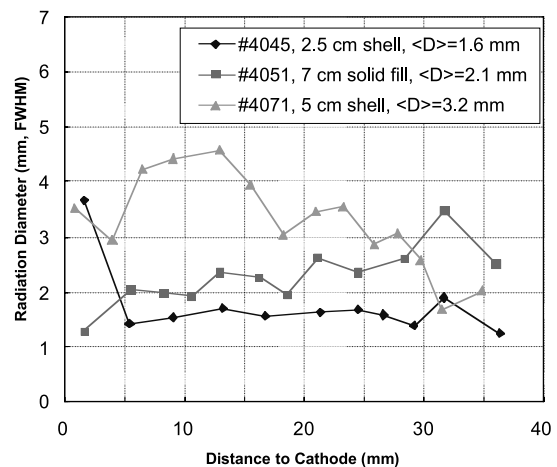| Double-EAGLE generator mode gas puff	60 kV, 100 ns 2.5-cm shell	60 kV, 200 ns 7-cm solid-fill
Implosion time (ns)	100	180
Peak current (MA)	3.4	3.5
K-shell X-ray yield (kJ)	21	11
X-ray pulse width (ns FWHM)	7	12
X-ray power (TW)	3.2	0.9
Total radiated yield (kJ)	140	130

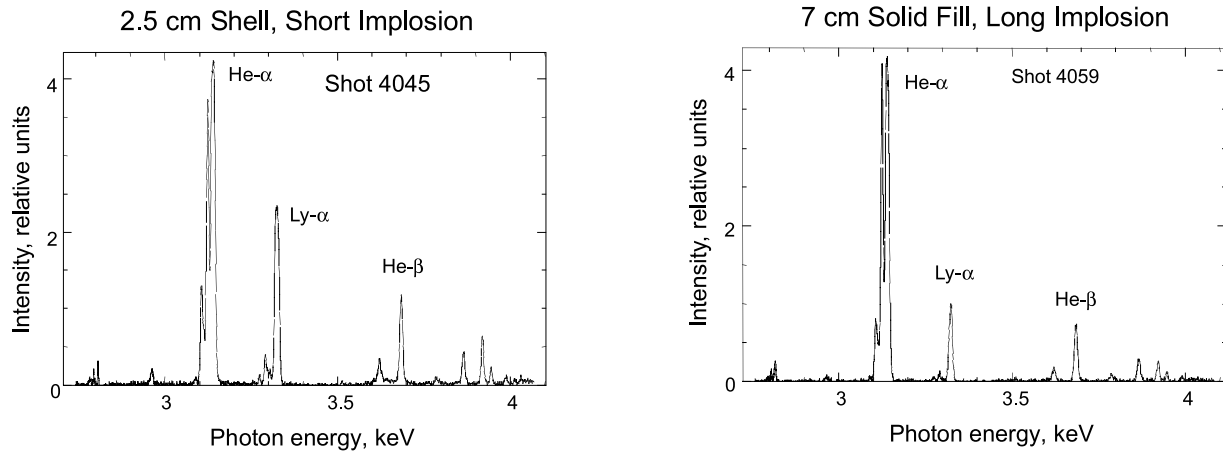**Fig. 9.** *K*-shell radiating diameters for long- and short-implosion PRSs.

Fig. 10. Time-integrated argon *K*-shell spectra for short- and long-implosion PRSs.

The core shows a ~60% decrease in electron density between short- and long-implosion PRS, and a ~30% decrease in radiating mass. The chlorine data give consistently higher density than argon and also a greater difference between long and short implosions. Again, we believe that opacity in the argon halo outside the core gives an underestimate of density, while the chlorine density diagnostic has low sensitivity and high error. Nevertheless, the true density in the long-implosion PRS appears to be lower by a factor ~2. This result confirms our expectations that larger initial diameters require higher compression ratios to maintain the desired final densities in longer-implosion PRS.

3.1.4. 10-cm solid fill experiments on Double-EAGLE

To take full advantage of the maximum current that will be available on DQ, the PRS load will need to have an implosion time close to 300 ns. To maintain the implosion velocity, this will require an even larger load: 10 cm diameter or more. We performed a limited number of tests with a 10-cm-diameter nozzle to see if there were any serious stability issues. With a peak current of over 4 MA and an implosion time of 247 ns, 7.3 kJ of *K*-shell radiation were produced with a 20-ns FWHM radiation pulse. (Note that the current drive for this configuration of Double-EAGLE, Fig. 12, is not at all like the expected linear ramp for DQ.)
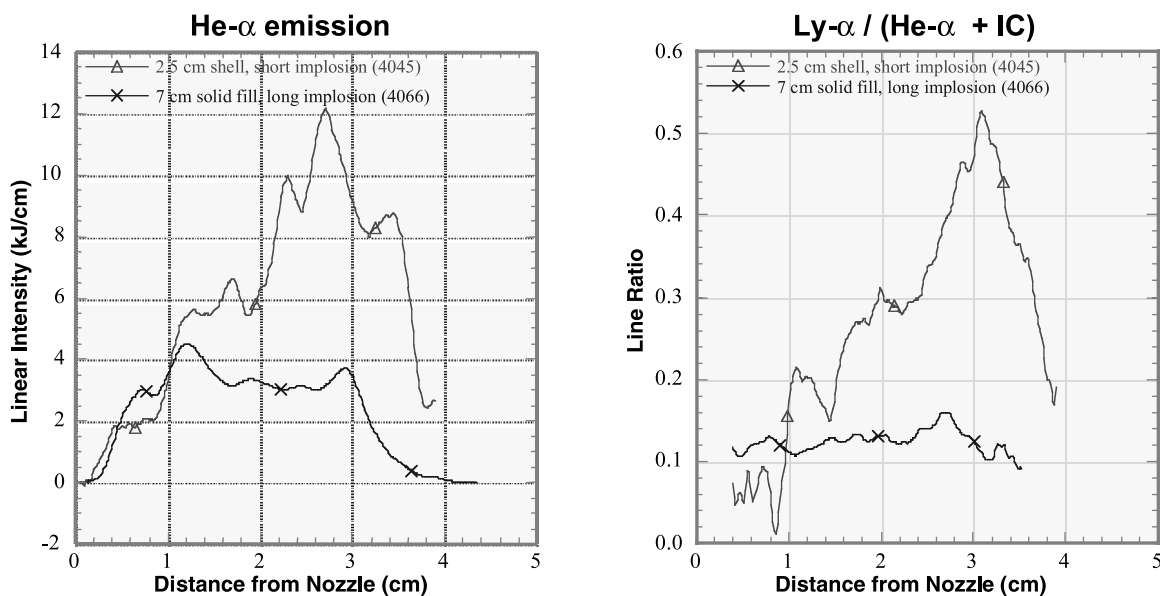

Fig. 11. Spatially resolved spectrograph confirms better axial uniformity with solid-fill gas puff.

Table 3. *Comparison of plasma conditions for short- and long-implosion PRSs.*

Generator mode gas puff	60 kV, 100 ns 2.5-cm shell	60 kV, 200 ns 7-cm fill
Ar electron density (10^{20}cm^{-3})	5.1	2.1
Cl electron density (10^{20}cm^{-3})	13	5.1
Ar electron temperature (keV)	1.9	1.45
Cl electron temperature (keV)	1.2	1.1
Cl ion temperature (keV)	16	22
K-shell radiating diameter (mm FWHM)	1.6	2.1
K-shell radiating mass (μg/cm)	43	30

Pinch quality was good; compare the optical framing images (4-ns exposures), Figure 13, viewing the pinch axially, with the comparable view of the 7-cm-diameter load, Figure 14. The initial images for the 10-cm-diameter load are slightly elliptical. Because the magnetic field lines resist "bending," such azimuthal asymmetries are not expected to grow and become unstable.

4. DOUBLE-SHELL GAS PUFF EXPERIMENTS ON DOUBLE-EAGLE AND SATURN

Recent *z*-pinch experiments have reported improved X-ray output with nested wire arrays (Deeney *et al.*, 1998*a*) and double shell gas puffs (Baksht *et al.*, 1998). The rationale for a double shell configuration is that the interaction of the imploding outer shell with the inner shell suppresses Rayleigh–Taylor instabilities developed during the implosion time of the outer shell (Golberg & Velikovich, 1993; Book, 1996; Hammer *et al.*, 1996; Velikovich *et al.*, 1996). The level of suppression depends on the thicknesses and densities of both shells. Based on such considerations, we designed and built a new double shell nozzle driven by a dual plenum valve (Song *et al.*, 2000). Here we discuss the *z*-pinch results achieved on Double-EAGLE and Saturn.

4.1. Double-EAGLE experiments with the double shell

Our initial double shell experiments were performed on Double-EAGLE configured for a 200-ns short-circuit rise time with a peak current of 4 MA. Figure 15a is a photograph of the shell-on-shell gas nozzle. The valves of each shell operate in unison but each shell has its own plenum. Pinch length was 3.8 cm. The gas density profile is shown in Figure 15b. As expected, near the nozzle (2 mm), the flow consists of two distinct shells. By 38 mm from the nozzle face, the divergences in each shell make the net density distribution more nearly uniform with radius.

4.1.1. Summary of Double-EAGLE double shell results

Figure 16 is a sample of the current drive and *K*-shell power of a typical shell-on-shell implosion. As summarized in Sze *et al.* (2000), the double shell results are on a par with the performance of the 7-cm solid-fill gas load. Using the measured gas profile and measured current, the observed and calculated implosion times are in good agreement. Optical images (Fig. 17; compare with Figs. 13 and 14) show that the outer shell implodes with good azimuthal symmetry. At $t = -39$ ns from the peak *K*-shell power, the fourth image, the outer edge of the inner shell is just beginning to light up. This implies that there is no significant current flowing on the inner shell until the outer shell collides with it. (The features inside of a 4-cm diameter around the axis, seen in the third and fourth frames, are scattered light off the surface of the central stub of the nozzle.)

The predictable behavior of these pinches is clear in the correlation between the optical image radius, as seen in Figure 17 and the predicted position of the snowplow using a simple 1-D code; see Figure 18. Likewise, the zippering of the pinches is fairly well (Fig. 19) reproduced by the snowplow calculations. These results imply that we know where the initial mass and current are, and that there are no significant mass losses during the implosion.

Each shell has an independent gas plenum. Thus we can trace the origin of the *K*-shell radiation. For some shots, we
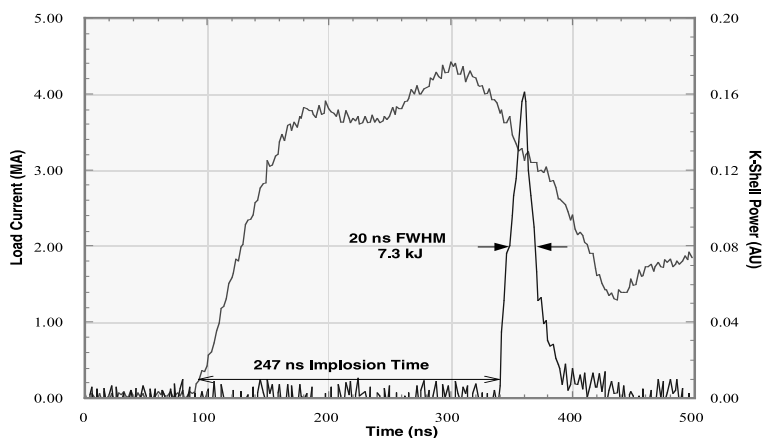

Fig. 12. Current and K-shell power for 10-cm-diameter solid fill (#4459) on Double-EAGLE.

-89 ns   -68 ns   -46 ns

Times with respect to start of K-power, shot 4403; peak K-power @ +12 ns

Anode Wires

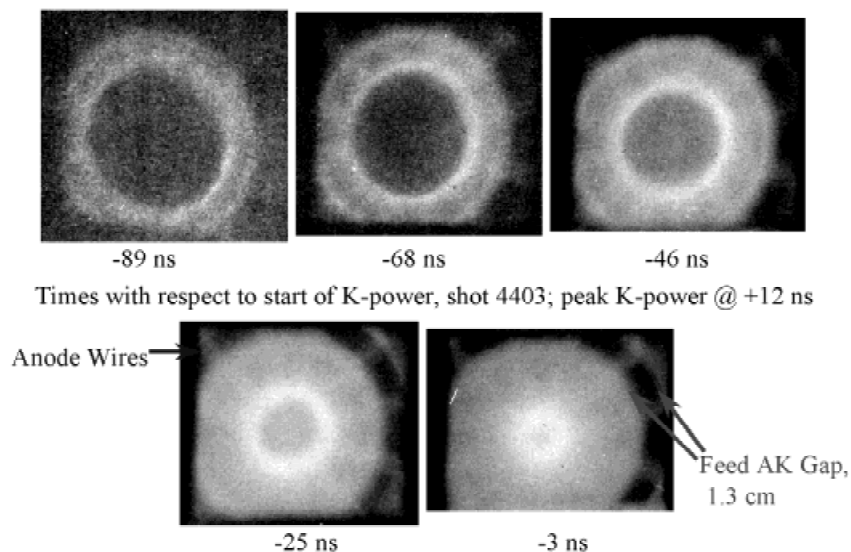-25 ns   -3 ns

Feed AK Gap, 1.3 cm

Fig. 13. Optical framing images for the 10-cm solid fill on Double-EAGLE.

used a 98% Argon and 2% Freon-12 (CCl_2F_2) gas mixture in the outer shell and 100% pure Argon in the inner shell. For other shots, we interchanged the gases in the two shells. With the chlorine tracer present in the inner shell only, the chlorine Ly-α line was observed easily. As seen in Table 4, for the shots with chlorine in the outer shell, the chlorine Ly-α like emission was at least 4.5 times weaker.

Deeney *et al.* (1995) and Apruzese *et al.* (1998) have demonstrated for wire array implosions that the center of a *z*-pinch is at the highest temperature. Likewise, MHD models of *z* pinches predict a hot core. Hence our chlorine data imply that the hottest part of the pinch, that is, the on-axis mass, is supplied predominantly by the inner shell. Some mixing of the two shells due to the R-T instability probably takes place. But the data imply that there is no significant penetration of the outer shell mass into the core of the inner shell mass that produces most of the observed *K*-shell output. In combination with snowplow stabilization, we expect that the outer part of the inner shell is very effective at smoothing out the bubbles and spikes of the incident outer plasma shell. Hence mixing would occur only near the boundary between the shells.
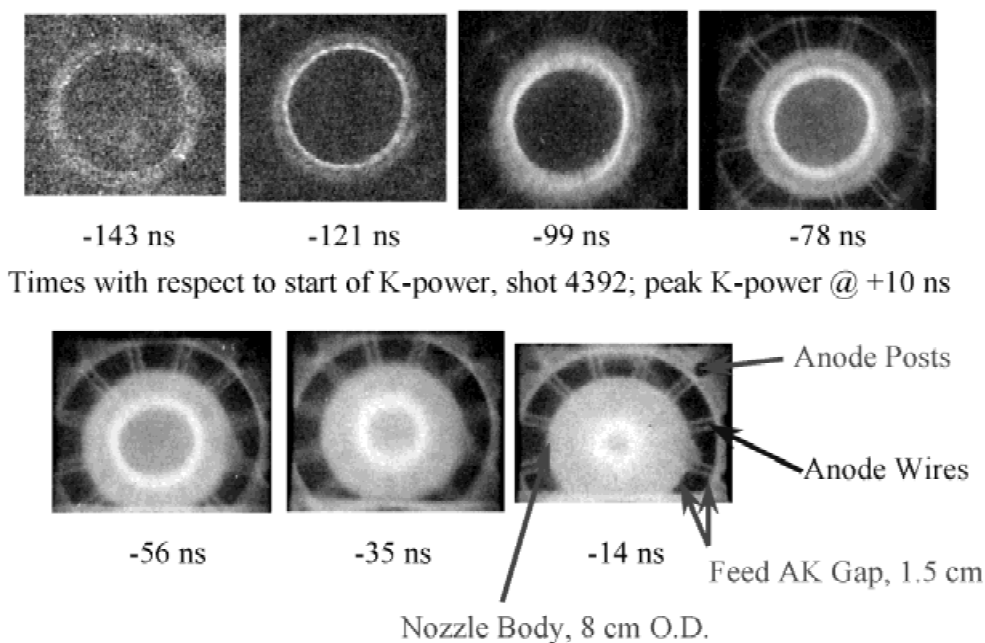

-143 ns   -121 ns   -99 ns   -78 ns

Times with respect to start of K-power, shot 4392; peak K-power @ +10 ns

-56 ns   -35 ns   -14 ns

Anode Posts

Anode Wires

Feed AK Gap, 1.5 cm

Nozzle Body, 8 cm O.D.

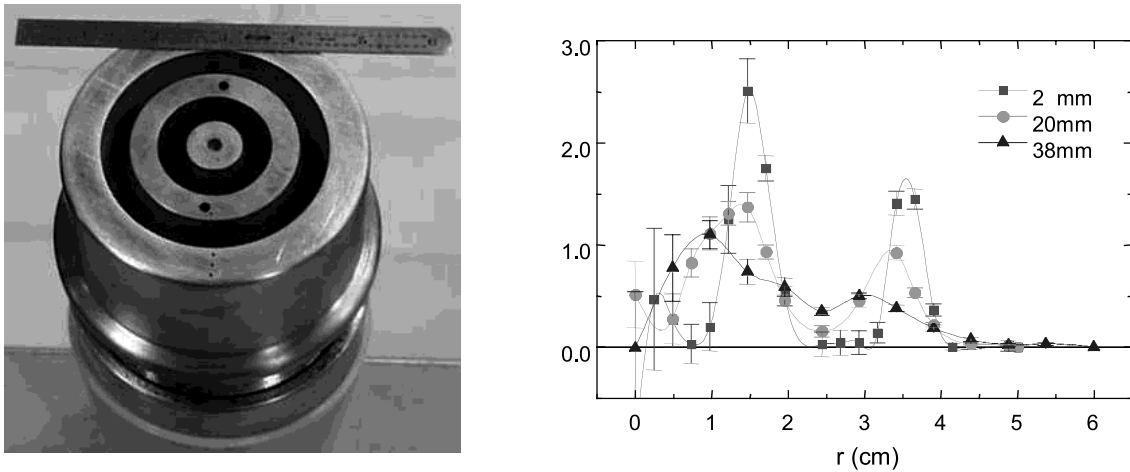**Fig. 14.** Optical framing images for the 7-cm solid fill on Double-EAGLE.

Fig. 15. (a) A photograph of the shell-on-shell gas nozzle. The inner and outer radii of the outer nozzle exit are 3 and 4 cm; the inner nozzle exit radii are 1 and 2 cm. (b) Argon radial density profiles of the shell-on-shell nozzle at 500 μs flow time.

4.1.2. Load length experiments with the double shell

For the Saturn tests of the double shell, we had to use a pinch length of 2 cm (see Section 4.2 below) compared to 3.8 cm on Double-EAGLE. To see if we should expect better results on Saturn with a pinch >2 cm, we made a limited study of the effects of pinch length.

Based on modeling considerations (Section 2), yield per unit pinch length should primarily depend on the current driving the pinch. Since the electrical driver (e.g., Double-EAGLE or Saturn) has a fixed inductance of order 10s of nanohenries, a reduced load length means proportionately reduced load inductance and higher load current. Yield varies as at least the square of current and as the length, thus one expects that there should be an optimum length. For short loads where the load inductance is small compared to the generator impedance, yield should increase as length increases. For long loads where the load inductance domi-

nates, yield should decrease inversely with length to the power $(x-1)$ where x is 4 in the "inefficient" I^4 regime and x is 2 in the "efficient" I^2 regime. The optimum length corresponds (roughly) to

$$(\text{Generator Inductance})/(\text{Load Inductance}) \sim x - 1.$$

Hence on Double-EAGLE ($\sim$20 nH), we might expect that for the double shell (return cage radius of 6.8 cm, outer shell radius of $\sim$3.5 cm), the "best" load length is $\sim$5 cm. This oversimplified treatment, which ignores the dramatic change in load inductance during the pinch, implies that Saturn should benefit from equally long pinches if power flow problems do not dominate. A competing effect is that not all parts of the pinch radiate equally well. In particular, the most shell-like gas flow near the nozzle emits less than the more filled-in regions.
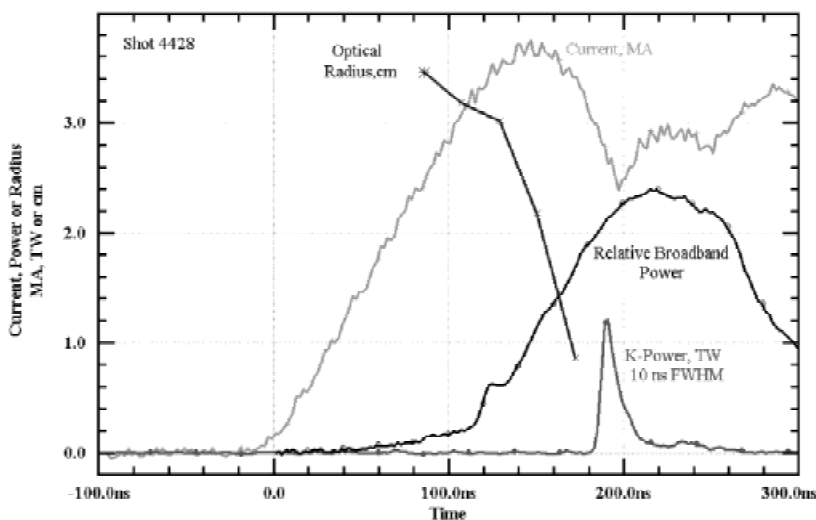

Fig. 16. An overlay of the measured current, optical image radius, and X-ray powers pulse for Shot #4428, a typical double shell implosion. The "broadband" relative power is from a bare XRD; the "step" at 120 ns is characteristic of the double shell—it is not seen with uniform fill loads.
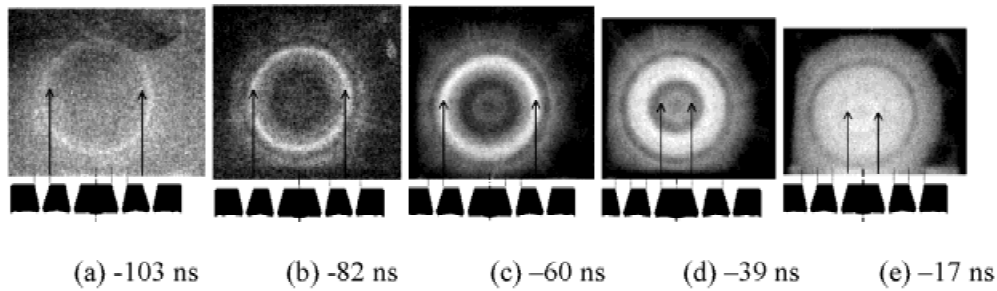
Fig. 17. Optical pictures of the double shell implosions in the radial direction: (a–c) initiation and acceleration of the outer shell; the arrows mark the 6-cm ID of the outer shell, (d) collision of the outer shell with the inner shell; outer edge of inner shell is just beginning to light up at this time, and (e) final implosion of the combined shells. Sketches of the nozzle under the pictures are shown to illustrate the position of the plasma shells. In (d–e), the arrows mark the 2-cm ID of the inner shell. Times are relative to peak *K*-shell power.

On this basis, we conducted a limited series of Double-EAGLE shots using pinch lengths of 2.0 cm, 3.9 cm, and 5.8 cm. The yield *versus* implosion time plot, Figure 20, indeed implies that the optimum length is probably between 3.9 cm and 5.8 cm for Double-EAGLE. Our simple analysis above argues that longer pinches should also be favored on Saturn where argon is becoming "efficient." (The limits of this analysis are shown in Fig. 21 where we see that our assumption that yield scales as length and I^4 is only roughly correct.)

4.2. Saturn experiments with the double shell nozzle

With testing time limited, we kept the same ratio (1 to 1) of inner to outer shell masses as employed on most of the Double-EAGLE shots. We had to reduce the pinch length to 2 cm, that is, reduced load inductance, to get good power flow. In accordance with the usual kinematic arguments, we found that the product of peak current times implosion time ($I * t$) scaled as the square root of plenum pressure, that is, as the square root of mass.

The sample current and *K*-power waveforms in Figure 22 hint at one important difference between the Double-EAGLE and Saturn tests: that is, the optimum implosion time on Saturn was smaller. This is made even more evident in the yield summary of Figure 23.

The minor differences in the current waveforms of the two machines cannot explain this; in fact, current peaks 20 ns later on Saturn compared to Double-EAGLE. A possible explanation lies in the higher mass (roughly three times higher) needed for the Saturn shots. The main emission lines of argon are certainly optically thick in the Saturn shots. Reduced implosion time *via* reduced mass may allow more of the *K*-emission to be radiated. This is in accordance with the detailed 1-D rad-hydro calculations of NRL; see also Apruzese *et al.* (1998). They show that higher implosion
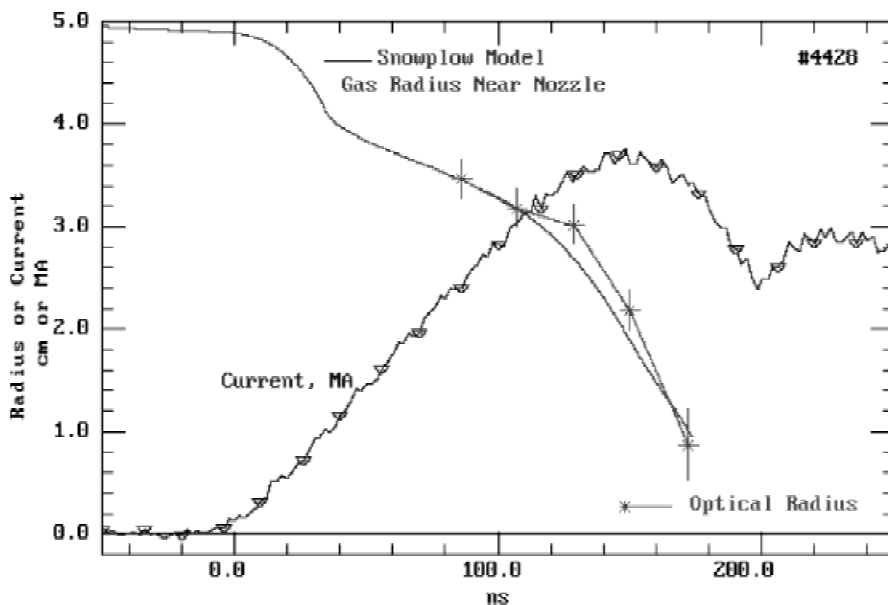

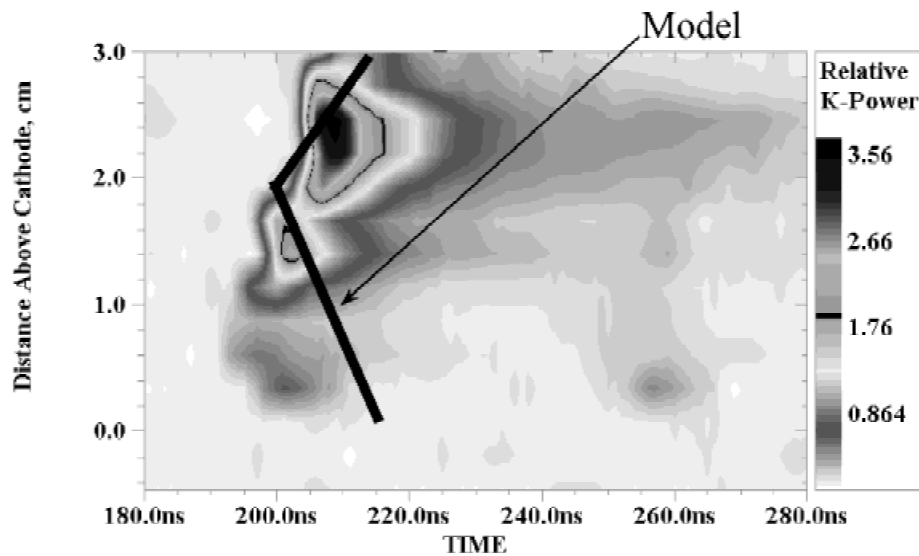**Fig. 18.** Observed and predicted radii of the double shell implosion front.

Fig. 19. Observed and predicted zippering for shot 4411. (Gas flow time of 400 μs.)

velocity (higher η or lower implosion time) is favored as load mass increases. The recent success of this nozzle in 110-ns implosions on Z at 15 MA (Sze *et al.*, 2001) is further support for this explanation.

5. EMPIRICAL SUMMARY, ANALYSIS, AND SCALING TO DQ

Earlier experiments on a number of different generators (Saturn, ACE-4, PITHON, DM2) have hinted that the X-ray yield from a PRS tends to decrease with longer implosion times, at least when the load is inefficient. Adding the data from our experiments per Sections 3 and 4, Figure 24 indeed shows that the best yield per unit pinch length for "long" implosion times lies a factor of roughly 2 below the short-implosion scaling lines. The trend is, however, not exact. At low currents on DM2 and GIT-12, 300-ns implosions seem to lie on the 200-ns trend line set by the ACE-4 and Double-EAGLE data. The Saturn data "long" pulse data

actually refer to implosion times of 150 to 180 ns. And Saturn "short" pulse is actually 70 ns. (In view of the wide range of test beds and methods used at various laboratories, the correlations between their results as seen in Figure 24 is impressive. Each lab uses different types of yield and current sensors, calibrated in unique ways. Yield per centimeter is derived from the physical length of the anode-cathode gap, not the length of the pinch that actually lights up well.)

This implosion time "penalty" quantifies the challenge for the development of new *z*-pinch facilities. The lower cost of "slow" pulsed power like DQ must be balanced against the lower apparent yield of long implosion time, moderate *Z* (>17) PRS loads. Remember however, that models suggest that this penalty may only apply in the inefficient regime. At higher currents (>8 MA for argon), implosion time should be less important as a yield determinant if large loads are not seriously disturbed by instabilities.

Table 4. *Comparison of plasma conditions for selected double shell tests*

| Test number and tracer location	*K*-shell yield (kJ)	*K*-shell ave. dia. (mm)	Electron temp. (keV)	Argon ion density (#/cc)	*K*-shell radiating mass fraction	Intensity Cl Ly-alpha w.r.t. Argon He-beta
Shell-on-shell						
4413, Cl both	11.2	2.7	1.42	1.2E + 19	0.25	16.5%
4428, Cl inner	12.0	3.1	1.48	1.1E + 19	0.49	13%
4421, Cl outer	9.9	1.9	1.45	2.2E + 19	0.26	2.8%
4429, Cl outer	9.1	3.8	1.52	0.65E + 19	0.52	1.8%
7 cm solid fill:						
4432	10.9	2.5	1.45	1.4E + 19	0.47	11.2%
Estimated ± uncertainties:	1 kJ	0.2 mm	0.04 keV	20%	0.15	1%
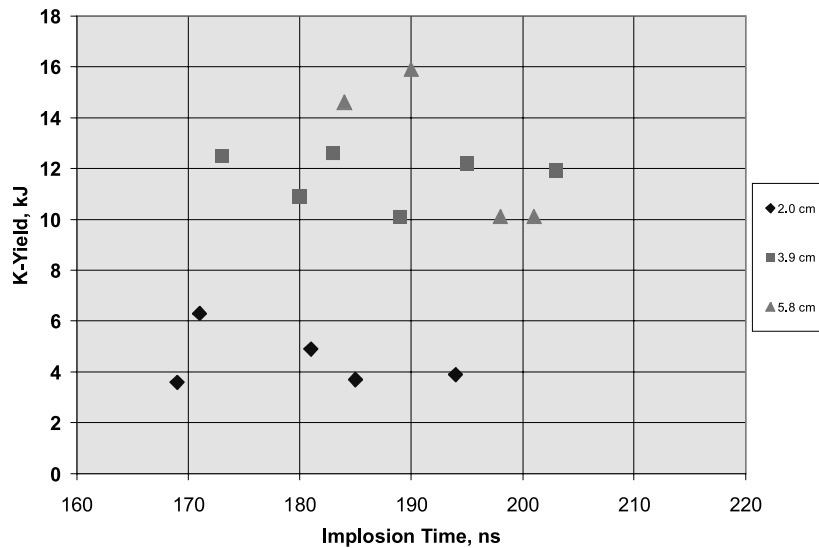
Fig. 20. Yield *versus* implosion time for the double shell length scans on Double-EAGLE.

5.1. Analysis

Our experiments have also given us insights into the plasma conditions that underlie the decrease in yield with implosion time, so that future theory and experiment can be directed towards mitigating the physics that are presently limiting the X-ray output from long-implosion PRS. As discussed in Section 3.3, the most significant difference in plasma conditions in the *K*-shell radiating core are the 2.5× decrease in density and 1.4× decrease in mass for long-implosion PRS compared to short implosion time tests. Within experimental error, the respective electron (and ion) temperatures show no significant difference. At constant temperature and neglecting opacity effects, the X-ray power then scales as the product of electron and ion densities with core plasma volume (V), or as the product of density and radiating mass:

$$P \propto n_e n_i V \propto n_e m_k$$

These factors account for most of the 4× reduction in power and 2× reduction in yield, allowing for the 2× increase in pulse width.
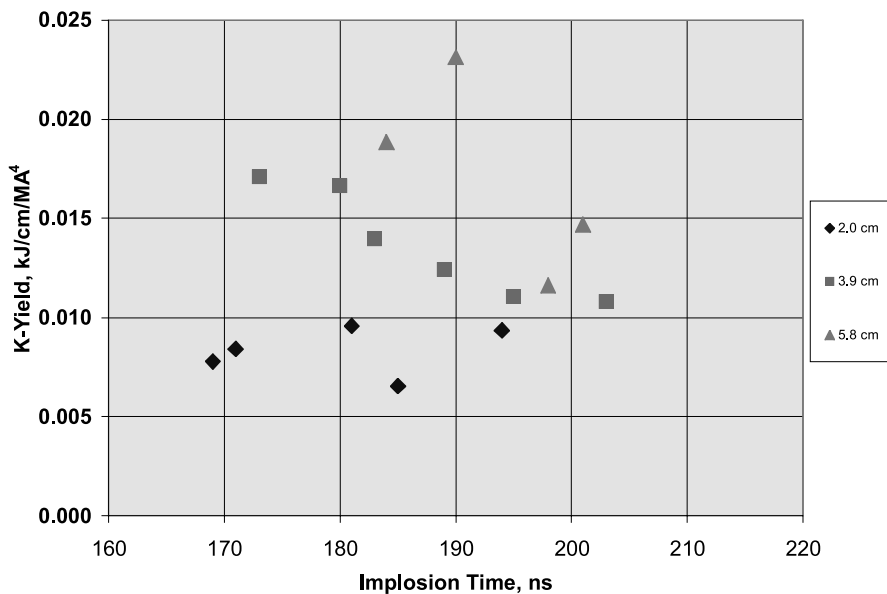

Fig. 21. Yield per centimeter of pinch per current to the fourth power for the Double-EAGLE length scan. In the absence of instability losses for the shell-like gas flow near the nozzle, this parameter should be constant as a function of length.
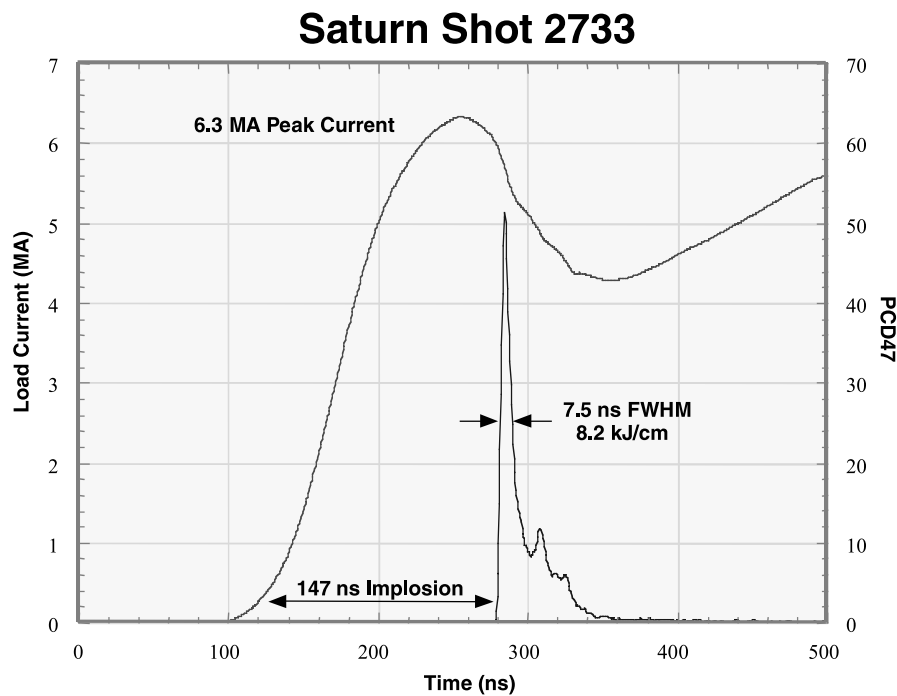
Saturn Shot 2733

Fig. 22. Example of Saturn Current and Double Shell *K*-Power.

The decreased density of the long-implosion PRS is related to the requirement for higher compression ratio to achieve the same final radius as short-implosion PRSs, which have a smaller initial radius. Since that 2.5-cm "shell" and 7-cm solid-fill gas puffs have similar masses, the 1.3× difference in final diameter accounts for most of the difference in density. It is illustrative to define the compression ratio as the ratio of the mass-weighted mean initial diameter to the FWHM radiating diameter. The 7-cm-diameter solid-fill has mean initial and radiating diameters of ~40 mm and 2.1 mm, respectively, giving a compression ratio of 19. From the interferometric characterization of the 2.5-cm-diameter shell, the initial mean diameter (defined per Section 2) at the 2-cm distance from the nozzle where it radiates best is 22 mm. Thus the 1.6-mm radiating diameter corresponds to a compression ratio of 14. We see that the long-implosion PRS has a higher compression ratio, but it needs to be higher still.

The essence of the implosion time penalty then seems to be some limit on compression ratio or final pinch diameter. The origin of such a limit is not completely clear. One can imagine that the thickness of the imploding "sheath" may control the final pinch dimension. Perhaps sheath thickness
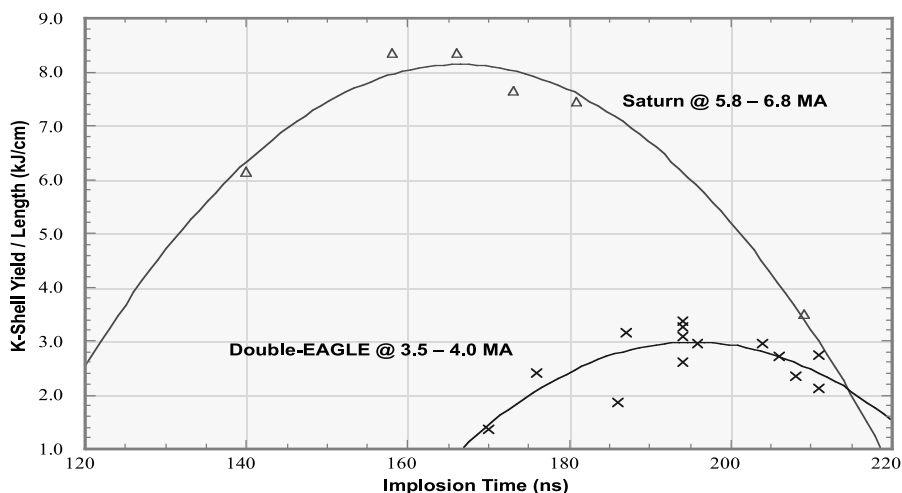

Fig. 23. Double shell yield *versus* implosion time for Double-EAGLE and Saturn.

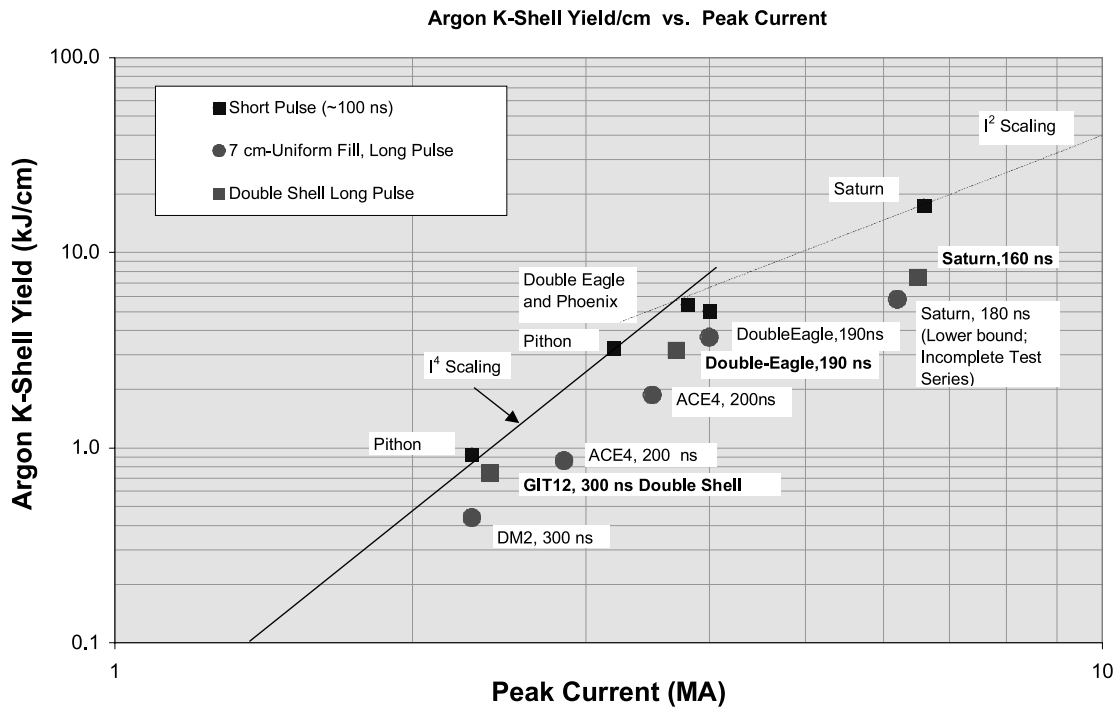**Argon K-Shell Yield/cm vs. Peak Current**

Fig. 24. Argon *K*-shell yield scaling for short- and long-implosion PRSs.

does grow with time. But one would also expect that the radiation pulse width would also be correlated with the sheath thickness. The *K*-power data show that pulse width is not uniquely controlled by implosion time.

The hydromagnetic Rayleigh–Taylor instability can broaden the sheath of an imploding *z* pinch and, thus, limit the compression and density that can be achieved. A two-dimensional simulation of thick-shell and solid-fill gas puff PRSs with realistic density profiles shows that axial density gradients provide the initial perturbation (Roderick *et al.*,

1998). The R-T instability grows only in the sheath between the magnetic piston and the shock front driven ahead of it, and mass accretion from the snowplow saturates the instability at small amplitude. Although exponential growth resumes in the shell when the snowplow reaches the inner surface, the R-T modes continue to grow slowly (i.e., less than exponentially) for the solid fill.

Time-resolved imaging indicates that two-dimensional effects are significant in both the short- and long-implosion PRS. Figure 25 shows a sequence of *K*-shell images for the
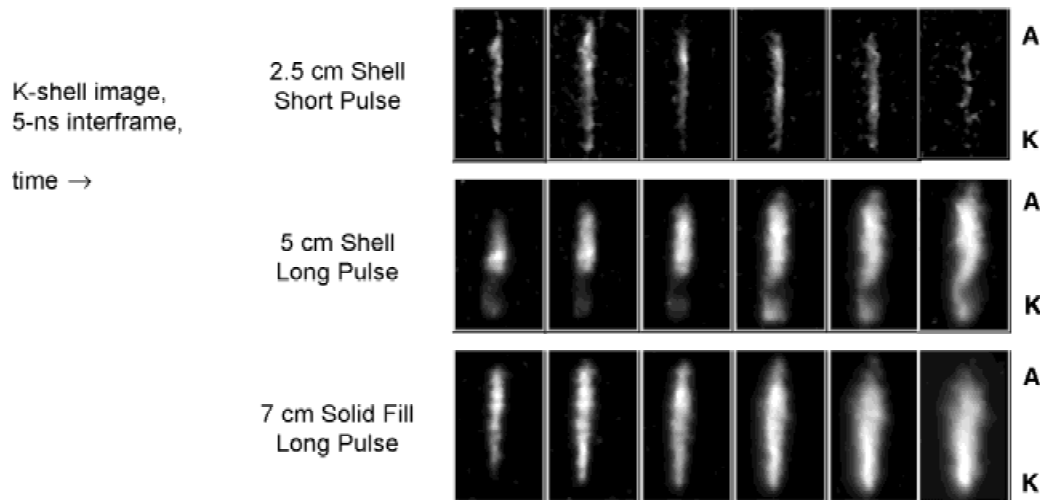

Fig. 25. Time-gated X-ray images show evidence of 2-D (and 3-D?) effects.

short-implosion PRS and both shell and solid-fill long-implosion PRS; time increases to the right with a 5-ns inter-frame time. All the pinch images show significant two-dimensional effects (e.g., $m = 0$ "sausages"); the 5-cm shell also shows a kink mode near the cathode that may even be three-dimensional. These images suggest that the instabilities are not growing rapidly during the K-shell radiating phases and that they are probably saturated remnants of an imploding R-T instability rather than a magnetohydrodynamic instability in the stagnated pinch. Additional measurements are needed to confirm this hypothesis, and to determine the dependence of the growth and broadening upon implosion time and initial diameter.

6. PLASMA CONDITIONS DERIVED FROM X-RAY SPECTRA

We have measured plasma conditions for both standard short (100-ns) and longer (200-ns) implosion time argon gas puff loads. Our objective was to understand the effect of implosion time on z-pinch performance. The plasma parameters of interest were electron temperature, ion temperature, and electron density. Deriving both electron and ion temperatures gives a measure of how well the ion kinetic energy has thermalized. This thermalization is assumed to be 100% in the calculation of the η required for efficient radiation production. High electron densities are important to thermalization and efficient radiation. For 100-ns implosions, the gas profile was a 2.5-cm-diameter nominal shell, while both 5-cm-diameter shell and 7-cm-diameter solid-fill profiles were used for 200-ns implosions. Since the gas puff distributions vary both in r and z, spatially resolved measurements are desired; our initial measurements look at variations in z.

We find that the average electron density is well correlated with the imploded mass; electron and ion temperatures are not equal, hence thermalization is incomplete. We also find that a larger axial extent of the pinch radiates in the

K-shell for solid-fill profiles, and that the "shells" radiate most strongly in regions where their profiles approach a solid fill.

6.1. Approach

We use X-ray spectroscopy to determine plasma conditions. Electron density and temperature can be estimated from a combination of different line ratios. The absolute source yield and plasma dimensions can also be used. Two axially resolved spectrographs were fielded. One measured Ar emission using a PET crystal, and the other Cl using a Si(111) crystal. Cl was introduced to the gas puff *via* CCl_2F_2, which was added to the Ar at the 2% molecular level (thus the puff was 4% atomic Cl).

The argon spectra were analyzed in the way suggested by Apruzese *et al.* (1997). The Ly-α to He-α line ratio, the absolute brightness of the pinch in the K-shell, and the K-shell diameter, measured from a pinhole camera photograph, are used to estimate electron densities and temperatures. The absolute pinch brightness is found by summing the lines, normalizing to the measured K-shell yield, and dividing by the measured X-ray pulse width. Both the line ratio and K-shell brightness are resolved in z along the pinch axis. An atomic physics code must be used to predict temperatures and densities from the observed brightnesses and ratios because opacity effects are expected to be important.

The chlorine dopant provides a measurement that should be much less sensitive to opacity effects. Electron density can be estimated from the ratio of the resonance transition (He-α) of the helium-like ion Cl XVI to the intercombination line ($1s^2\,^1S - 1s2p\,^3P^0$). Because this ratio also depends on electron temperature, the temperature is estimated from the ratio of the He-α line to the dielectronic satellite transition ($1s^22p\,^2P^0 - 1s2p^2\,^2D$ or j, k, l satellites). If the Cl is optically thin, it could be Abel inverted to provide a radially-resolved measurement in the future. Glenzer *et al.* (1997) has used these ratios to diagnose plasmas with elec-
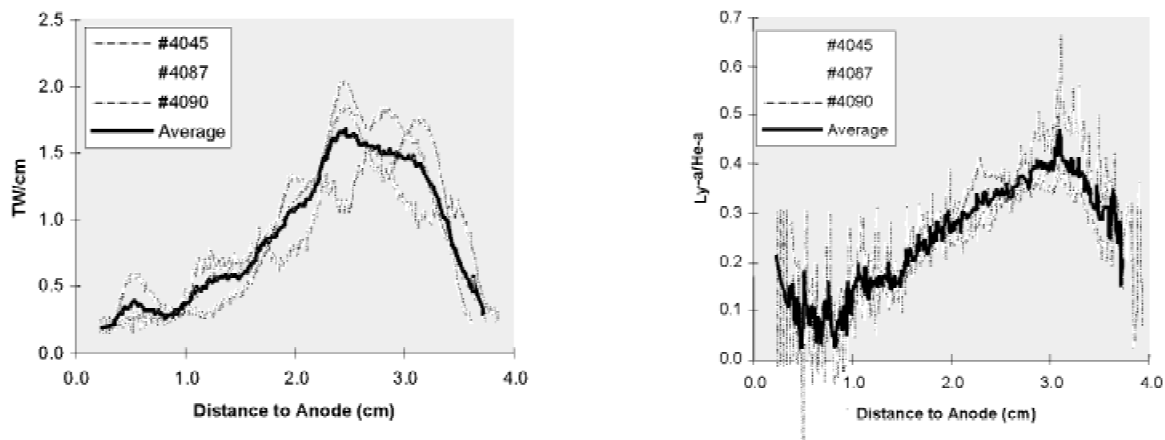

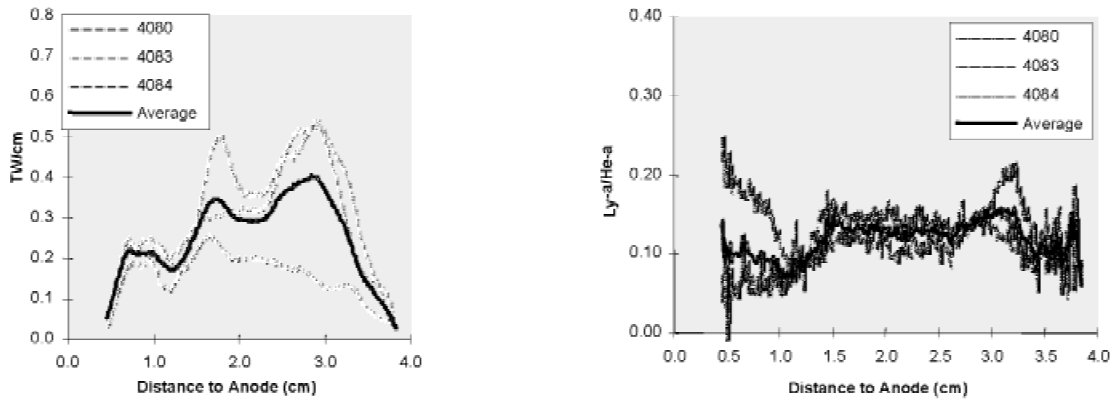**Fig. 26.** Emission and line ratio both peak toward anode for short-pulse 2.5-cm shell.

Fig. 27. Emission and line ratio are both more uniform for long-pulse 7-cm solid fill.

tron densities near 10^{21} e/cm^3 and electron temperatures between 1 and 3 keV. In our experiments, spectral dispersion is provided by a Bragg-diffracting crystal in the Johann geometry. A similar instrument was used by Wong to make measurements at the SATURN facility (Wong *et al.*, 1998). The Johann geometry eliminates source size broadening of spectral lines. By keeping the dopant level sufficiently low, opacity should not broaden the lines either. The remaining broadening will be due to Doppler and Stark effects. Given the electron density and temperature, the Stark and opacity effects can be compensated for and the Doppler contribution determined, giving an estimate of the ion velocities in the plasma. We have assumed that the ion velocity distribution is Maxwellian, and have used the intercombination line width to estimate the ion temperature.

6.2. Measurements

Both Cl and Ar spectra were obtained for a number of shots. Figures 26 and 27 show Ar *K*-shell emission and the Ar Ly-α::He-α line ratio as a function of the distance from the cathode for two different load configurations. Both the peak pinch brightness and line ratio are more than three times higher for short pulse than long pulse implosions.

The same line ratio and relative brightness for Cl can be compared with the Ar results (Fig. 28). The line ratios for long pulse shots agree very well, but there is a discrepancy for short pulse shots—the Ar ratio is a factor of two higher in the region of brightest emission. This is consistent with increased opacity, since the absorption of the He-like line should be much greater than for the H-like one.

We have used the Cl spectra to estimate plasma parameters as a function of *z*, the distance from cathode to anode, for two sample shots. In Figures 29 through 32, the electron and ion temperatures are shown on one plot, and the electron density and relative Cl emission are shown on the other.

To easily compare one configuration with another, we have calculated source-averaged plasma parameters. These averages were weighted by the sum of the two dominant Cl lines—the He-α and intercombination lines. A summary of the source-averaged plasma parameters is given in Table 5. The uncertainties in the source-averaged parameters are not due to measurement uncertainties, but rather variations in the parameters along the length of the pinch. The mean electron temperatures are comparable for the short-pulse shot and the 7-cm-diameter long-pulse shots, with the 5-cm shot coming in somewhat lower.
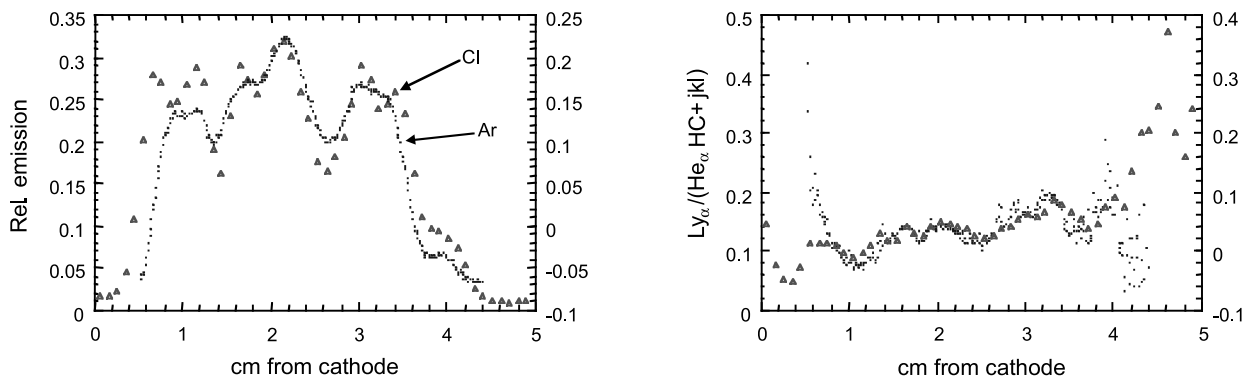

Fig. 28. Long-pulse 7-cm solid-fill brightness and line ratio traces are consistent between Ar and Cl.

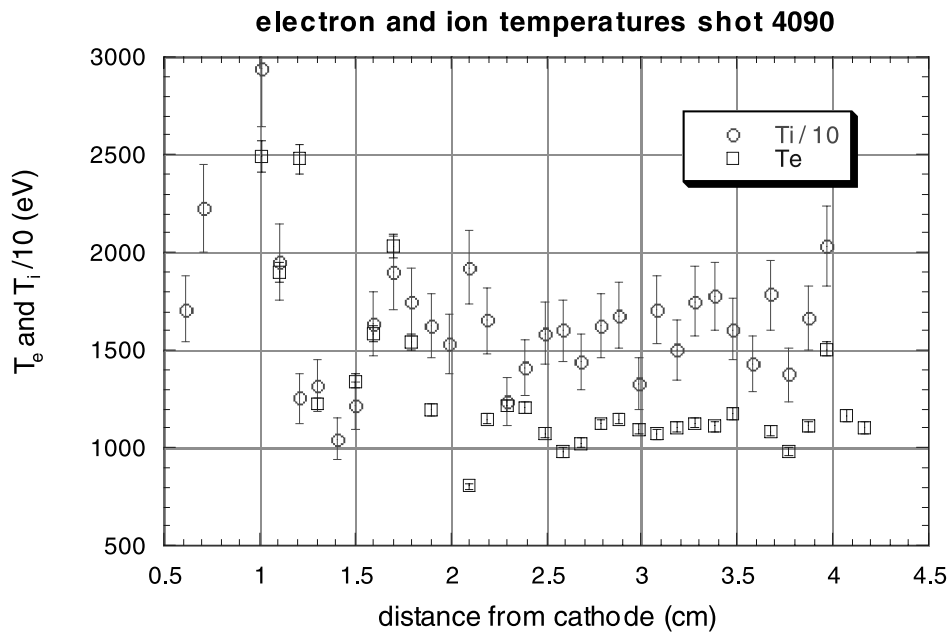**electron and ion temperatures shot 4090**

Fig. 29. Short-pulse (2.5 cm) temperatures are fairly uniform axially.

Comparing the *K*-shell power and yield with the estimated plasma parameters provides a consistency check that increases our confidence in the measurements. The relative emitted power for a transition to the ground state, I_{n0}, is given by

$$I_{n0} \propto \frac{\langle n_e^2 \rangle}{\sqrt{\langle T_e \rangle}} \exp(-\Delta E_{n0}/\langle T_e \rangle),$$

assuming that the ion charge state is not varying in the *K*-shell emitting region. The relative yield is found by multiplying I_{n0} by the radiation pulse width, $\langle \tau \rangle$, and the square of the *K*-shell emitting diameter, $\langle d \rangle$. Again, the pulse width and diameter used are averaged over the length of the source. As shown in Table 6, the estimated plasma parameters are consistent with the observed Ar yield (3.1 keV was used for ΔE_{n0}).
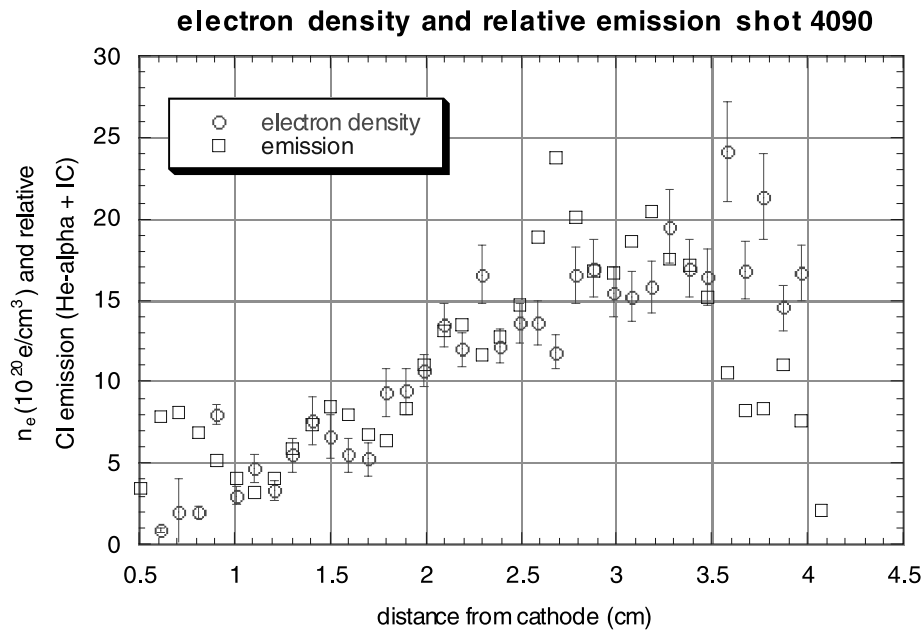
electron density and relative emission shot 4090

Fig. 30. Short-pulse (2.5 cm) emission and density peak toward anode, where gas profile is more filled in.

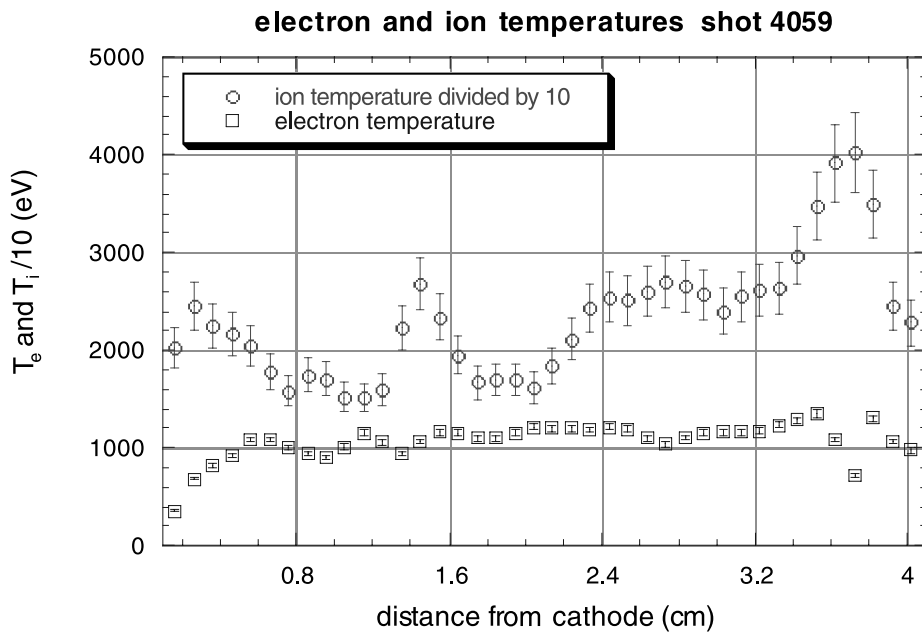**electron and ion temperatures shot 4059**

Fig. 31. Long-pulse 7-cm solid-fill T_e is fairly uniform; T_i has more variations.

6.3. Summary

Spectroscopic measurements have been used to estimate plasma temperatures and densities for Double-EAGLE Ar gas puff implosions. Implosions using both 100- and 200-ns rise time current pulses were analyzed. For the shell nozzles, most of the yield was produced between the middle of the pinch and the anode, where the gas profile approaches a solid fill. Ion thermalization was better for the smaller diameter, higher mass implosions, and electron temperatures between 1.0 and 1.2 keV were achieved on both the 2.5-cm-diameter, short-pulse and 7-cm, long-pulse shots. The mean electron density estimated for the *K*-shell emitting volume increased almost linearly with increasing load mass. A comparison between two shots indicates that the estimated densities and temperatures are consistent with the measured yield.
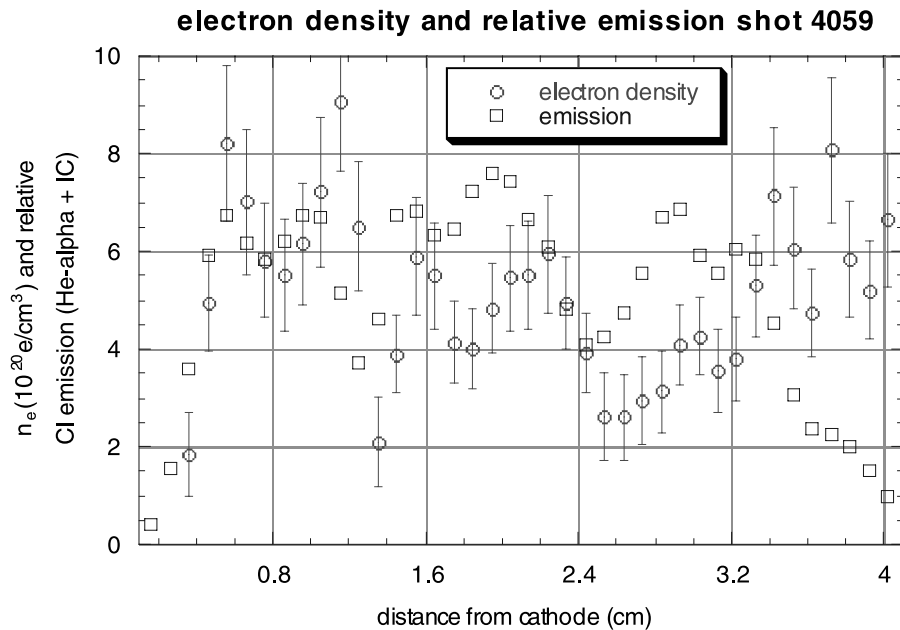
electron density and relative emission shot 4059

Fig. 32. Long-pulse 7-cm solid-fill density and emission are more uniform axially than shell.

Table 5. *Summary of plasma parameters from Cl spectra.*

Shot #	Nozzle diameter	Current rise time	Peak current	$\langle T_i \rangle$ (keV)	$\langle T_e \rangle$ (keV)	$\langle T_e \rangle / \langle T_i \rangle$	$\langle n_e \rangle$ (10^{21} e/cm^3)
4090	2.5 cm shell	100 ns	3.5 MA	16 ± 3	1.2 ± 0.3	$7.5 \pm 2.3\%$	1.3 ± 0.5
4071	5.0 cm shell	200 ns	3.5 MA	14 ± 4	0.77 ± 0.06	$5.5 \pm 1.6\%$	1.1 ± 0.3
4059	7.0 cm solid-fill	200 ns	3.5 MA	22 ± 5	1.1 ± 0.1	$5.0 \pm 1.2\%$	0.51 ± 0.16
4083	7.0 cm solid-fill	200 ns	4.0 MA	20 ± 4	1.0 ± 0.3	$5.0 \pm 1.8\%$	0.84 ± 0.25

7. DIAGNOSTICS DEVELOPMENT FOR LONG IMPLOSION TIME LOADS: INITIATION AND IMPLOSION IMAGING

With the success of small interwire gaps for high power wire array z pinches, it has become even clearer that it is important to correlate the initial stages of a pinch with careful diagnostics of the radiation performance of the load. Here we cover some diagnostics that have increased our knowledge of initiation and implosion phase dynamics for the gas puffs. First we discuss the use of an optical framing camera to provide visible light images of the initiation and implosion of z pinches. Second, a "zipper" array gives a one-dimensional image of the K-shell emission as a function of time and distance along the pitch. We show that the zipper behavior can be correlated with the initial mass distributions. Third, CCDs (charge-coupled devices) have been configured for use in the severe environment of pulsed power machines (Double-EAGLE and Saturn). Our results demonstrate that CCDs can return high quality data and are an attractive replacement for conventional film to perform X-ray 2-D imaging or spatially resolved spectroscopy. We conclude with brief details on a new preionizer design for more symmetric initiation of current flow on a gas puff.

7.1. Optical framing camera

The IMACON optical framing camera uses fairly old technology. The scene is imaged with standard visible light optics onto a photocathode sensitive between 450 and 600 nm. Gated electron optics (4-ns exposures) produce an image on an output phosphor that is then photographed. In the camera's framing mode, 8 to 12 images can be captured.

From spectroscopic studies, we know that the argon puff gas initially radiates in the characteristic lines of its neutral and singly ionized ions. Later in time, as the gas gets hotter and denser, the continuum becomes significant. The overall brightness of the pinching gas increases by many orders of magnitude during the implosion. Unfortunately, the camera has a limited dynamic range of roughly 100 at best. Hence it is difficult to capture good images of both the initiation of the pinch and its subsequent implosion. (On DM2 argon PRS shots with $\sim$1 kJ of K-shell yield, the observed surface brightness during the later stages of implosion was $\approx$100 W/ster/mm^2. At pinch time, surface brightness could exceed 1 kW/ster/mm^2. For Double-EAGLE shots, the surface brightnesses were about a factor of 10 higher.) To a limited degree, the effective dynamic range of the camera may be improved by using a narrow band filter that is centered on a characteristic line of the emitting gas. Initially, the filter passes the dominant line radiation. Later, the filter discriminates against the broad continuum. Thus for our experiments, we used a 10-nm FWHM filter centered on 480 nm which is reasonably matched to one of the dominant lines of singly ionized argon (Ar II) at 480.6 nm.

7.1.1. Optical framing images

The primary purpose of the optical framing data is to document qualitative features of the initiation and implosion of the z pinches. In particular, we are interested in perturbations that may seed instability growth leading to poor pinch compression and low radiation output. A typical image is shown in Figure 33. This single frame for Double-EAGLE shot 4070 shows the exit of the 5-cm-diameter "shell" nozzle, the anode return posts and the wire grid that defines the anode plane for the pinch. There are always 12 current return posts, but different nozzles have different bolt circle diameters for the posts. A pair of wires extends inward from the end of each post to define the anode plane. Like

Table 6. *Yield can be scaled from plasma parameters and dimensions.*

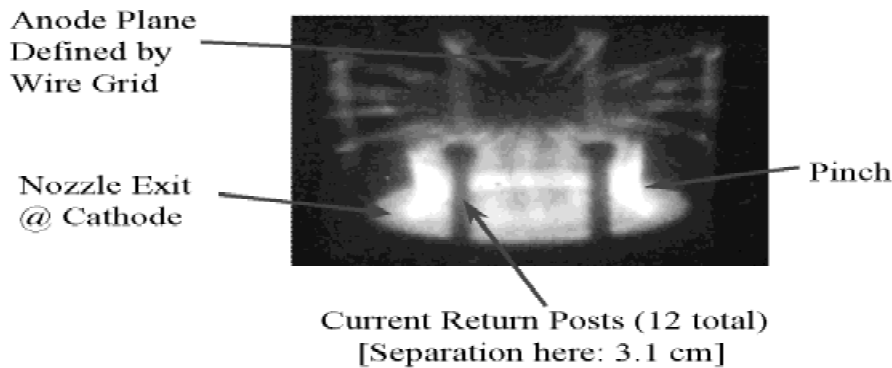| Shot #	Nozzle diameter	Current rise time	Peak current (MA)	$\langle T_e \rangle$ (keV)	$\langle n_e^2 \rangle$ (relative)	$\langle d \rangle$ (mm)	$\langle \tau \rangle$ (ns)	K-shell yield (kJ)	Scaled K-shell yield (kJ)
4090	2.5-cm shell	100 ns	3.5	1.2 ± 0.3	16.2	1.6	7 ± 1	20.0 ± 1.5	NA
4059	7.0-cm semi-solid	200 ns	3.5	1.1 ± 0.1	2.3	2.1	19 ± 1	11.2 ± 0.8	11.0

Fig. 33. Sample optical image on Double-EAGLE shot 4070.

most diagnostics on Double-EAGLE, the camera usually viewed the pinch at an angle of 68° from the pinch axis. On some shots, the camera viewed the pinch end on (0°); example images appear in Sections 3 and 4.

It is interesting to note that the images always show the light emission growing from the cathode across the AK gap to the anode plane on a 25- to 50-ns time scale. This behavior was seen for all Double-EAGLE, DM2, and ACE 4 argon shots. The cause for this is not completely clear. Presumably the emission is a function of gas density, electron density and electron energy. While the gas density is highest near the cathode, it cannot change much on a submicrosecond time scale. The electric field and current density are growing during these times. The sharp edge of the nozzle makes the electric field highest at the cathode. Understanding this might contribute to our knowledge of the current initiation process for gas puffs.

Many images, Figures 34 and 35, show axial filaments. The number of filaments, (≥ 20), is larger than the number of current return posts (12). The azimuths of the filaments are usually aligned with the pairs of chordal wires at the anode end of the pinch, which would produce 24 filaments. In this case the filaments may result from an initiation effect of the wires. Although the image resolution is not definitive, some filaments do not appear aligned with wires. Gas flow measurements have shown that puff valve asymmetries can persist in the supersonic flow, so it is possible that the filaments are related to the 18 holes in the puff valve aperture plate upstream from the nozzle throat. Comparable images for loads on other machines like ACE 4 do not show the same filamentary structure. Hence we may assume that changes in puff valve and nozzle design can control the presence of the filaments and in particular minimize or eliminate them.

Most of these optical images give mainly qualitative data on the pinch. In principle, we can get pinch diameter as a function of time for comparison with implosion calculations. Figure 36 is one example, showing four frames for a 7-cm-diameter uniform-fill load. The width of the emission at the nozzle exit systematically increases with time. Perhaps this emission is a measure of the thickness of the current sheath. Line-outs across the diameter are shown in Figure 37. Such data might be useful constraints on detailed MHD models of the implosion. (Also, some shots do give quantitative estimates of the pinch radius that correlate well with models; see Section 4 for an example.)

A final example of optical imaging of gas puffs appears in Figure 38 for the 5-cm shell load as used on DM2. The near 90° view allowed us to clearly see the development of the instability as the implosion proceeded. The bubble and spike structure is quite evident with a characteristic wavelength of about 4 mm.
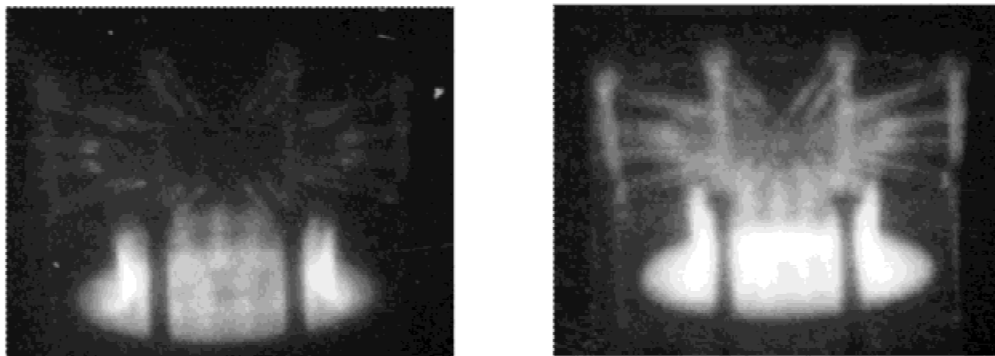

Fig. 34. Optical images of filaments for 5-cm shell long-pulse shot 4075; times are before peak *K*-power: left at −111 ns, right at −90 ns.
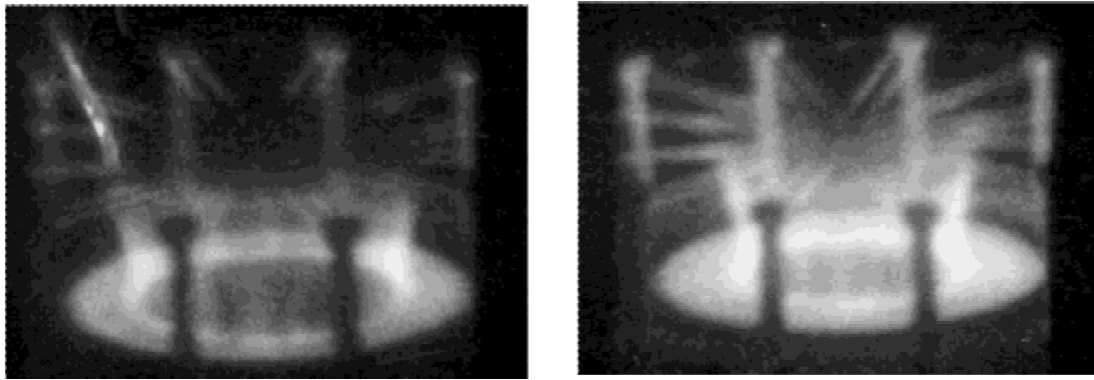
Fig. 35. Filaments evident in optical images for 7-cm uniform-fill shot 4063; the left frame at −117 ns and the right frame at −96 ns relative to peak *K*-power.

Optical imaging of aluminum wire shots (Fig. 39) also showed interesting features. We see bright-spot, on-axis emission well before *K*-shell emission. This is evidence for blow-off from the wires that reaches the axis very early ($\approx$100 ns) before the main implosion. The hot mass and perhaps some current that arrives on axis early may affect the main implosion.

7.1.2. Summary of load features seen in optical images

All gas loads on Double-EAGLE show axial filaments that may be related to details of the gas flow hardware. These filaments may affect the current sheath development and may be deleterious for the best quality implosions. Gas puffs also show visible emission growing from the cathode-side of the pinch on time scales of 10s of nanoseconds. This emission history gives us clues to the initiation process in gas loads and may affect how we model the implosions with 2-D MHD codes. Some images are good enough to give us quantitative data on current sheath thickness and diameter as a function of time. Again, such data could be useful in benchmarking detailed codes.

Optical imaging of the wire loads shows clear evidence of the arrival of hot emitting plasma on axis well before the main implosion. This observation is consistent with data from other experimenters who are studying the dynamics of wire PRS loads.

In summary, optical imaging has given us useful clues to initial and run-in conditions. In particular, the optical data should guide improvements in gas flow hardware and geometry. To a limited degree, the data also can provide useful
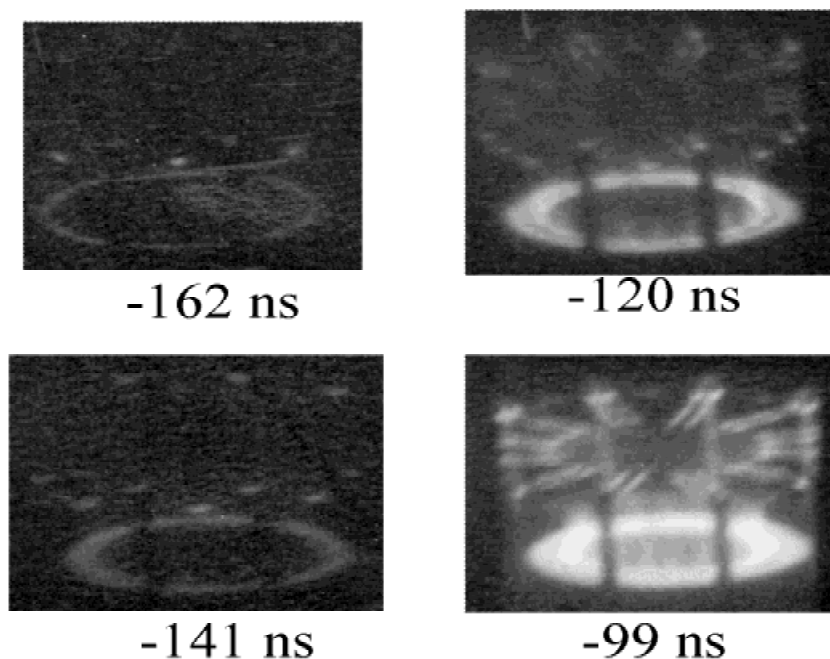

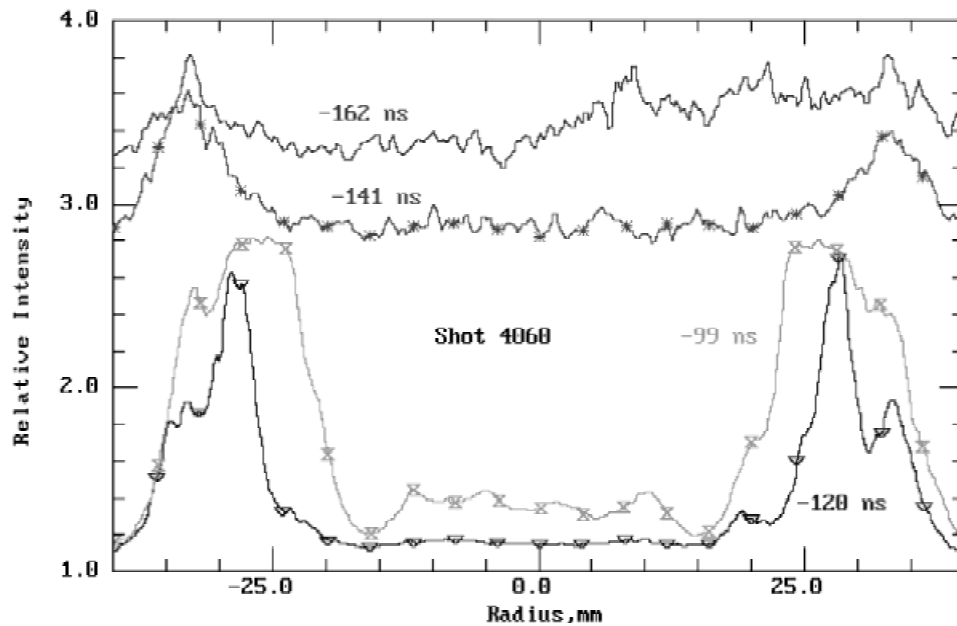**Fig. 36.** Optical images for 7-cm uniform-fill, long-pulse (165 ns) shot 4060.

Fig. 37. Line-outs for the optical images of shot 4060; the apparent sheath thickness increases from 3 mm at −120 ns to 6 mm at −99 ns.

constraints for modeling of the *z* pinches, especially current initiation and sheath development. Additional examples of the optical data appear in Sections 3 and 4.

7.2. 1-D imaging ("zipper") array

7.2.1. Diagnostic design and features

The zipper array gives a time-resolved one-dimensional image of the *K*-shell emission as a function of distance along the pinch. This diagnostic is especially useful in quantifying the "zippering" of the pinch, that is, the systematic variation of on-axis assembly time along the length of the pinch. While the zipper array lacks the spatial details of a 2-D microchannel plate (MCP) pinhole camera, the zipper array is very reliable, provides continuous time coverage, and is easy to use. Hence it is a good compliment to other pinch diagnostics.

Our zipper sensor uses a linear array of 14 silicon PIN diodes, positioned behind a perpendicular slit. The array axis is parallel to the pinch axis. The diodes are model AXUV-HS1 made by International Radiation Detectors (IRD). A very thin dead layer makes these diodes almost 100% quantum efficient for photons with energies between
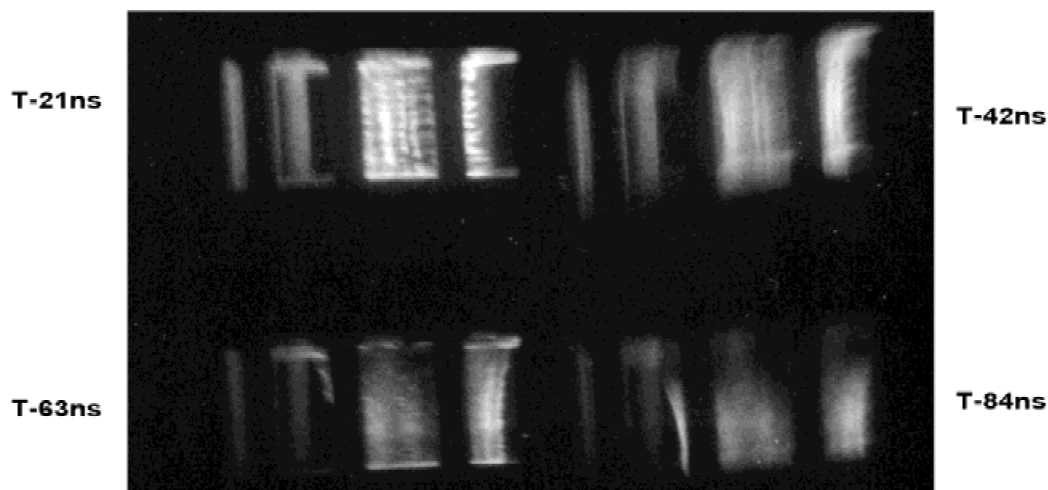

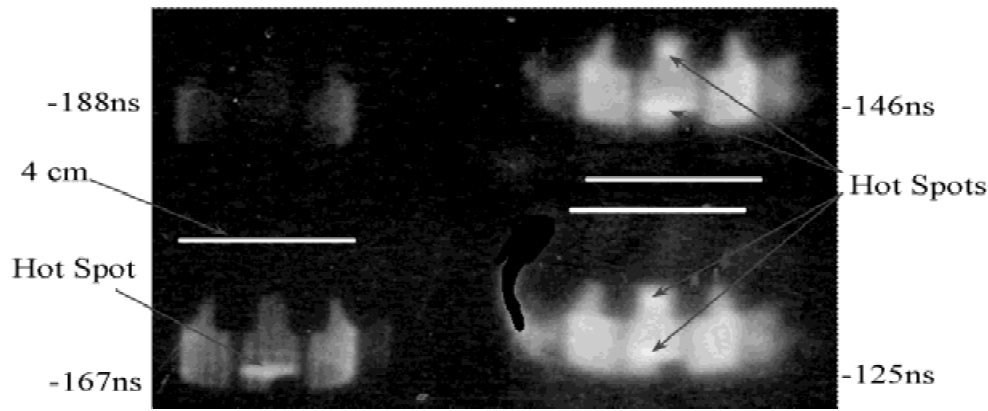**Fig. 38.** Optical images for the 5-cm shell load on DM2 shot 503.

Fig. 39. Optical images for a 4-cm aluminum wire array implosion, Double-EAGLE shot 4128.

$<$100 eV and $>$5 keV. The low junction capacitance gives each diode a rise time of 0.5 ns. With 1 ns/sample recording, each diode provides a continuous record of the K-shell power from a thin slice normal to the pinch axis. Unlike a gated camera, no time-critical triggering is needed. The diodes are very stable. Once the array and slit are aligned, operation is easy and maintenance is minimal. To establish the relative responses of the diodes, we make a "flat field" measurement: the imaging slit is replaced by a thick filter so that each diode has the same view of the pinch. This also lets us measure the relative timing between channels (cable and delay for each digitizer) to 1 ns.

One complication is the very high sensitivity of the diodes, which are essentially 100% quantum efficient. To keep peak signals below about 1.5 V (30 ma into 50 ohms) for good linearity, heavy filtration is needed. For the Double-EAGLE argon tests, we used a 5-μm-thick silver foil over each diode. The L-edge of silver at 3.38 keV just passes the dominant argon lines, Ly-α at 3.32 keV and He-α at 3.14 keV.

The net response to the pinch is a convolution of the filter transmission with the X-ray spectrum. For a typical argon spectrum, about half of the diode response is due to the K-shell lines. The rest of the response is due to the high-energy continuum above about 5 keV. Thus the zipper array is primarily sensitive to the very hottest parts of the pinch. The geometric optics of the array were chosen so that the array had a nearly contiguous view of the entire pinch with about 4-mm spatial resolution per diode.

7.2.2. Zipper data analysis

Because the zipper diodes are so different from the usual PRS diagnostics (XRDs, PCDs, etc.), it is important to demonstrate that the zipper data are consistent with other measurements of X-ray output. K-shell power waveforms as measured with XRDs, PCDs and the sum of the zipper diodes are usually in good agreement. This result is typical so long as the each zipper diode's peak signal is kept below about 1.5 V. Above that level, the zipper pulse width in-

creases because the peak current level ($\approx$30 ma) in the diode begins to saturate.

Having established some confidence in the performance of the zipper array, we turn to a review of its results. Figure 40 compares the zipper images for four consecutive shots with the short-pulse (100 ns), 2.5-cm-diameter nozzle. The objective of these shots was to hold gas injection constant and demonstrate the repeatability of the load. Gross features were indeed repeatable. The implosion time was 102 ± 2 ns. K-shell yield was 21.0 ± 1.0 kJ. The zipper data show that other features were also fairly reproducible. Only about 50% of the pinch length radiates well, typically the region farthest from the nozzle. This is where the gas flow is actually relatively uniform rather than shell-like. The variation of implosion time with distance above the cathode (the white line in each image) is almost constant, shot to shot. This implies that we have repeatable behavior in three different areas: gas injection and flow, gas breakdown and current initiation, and implosion dynamics.

Our initial purpose for the zipper array was to see if zippering was compromising the radiation output of the long implosion time loads, that is, if the differences in implosion time along the pinch axis are large compared to the thermalization time of each segment of the pinch. In that case, we would expect that the roughly spherical re-expansion of the first mass that arrives on axis would compromise the compression of adjacent parts of the pinch. The overall pulse width of such implosions would be controlled by the arrival time differences along the pinch axis rather than the intrinsic radiation time for a given element of compressed plasma.

Quantitatively, for a well-behaved implosion, we want the zipper "speed," that is, the slope of the lines drawn in Figure 40, to be larger than the implosion velocity. This is in fact what we observe for most of the loads tested. The zipper speed is well above 100 cm/μs while the implosion velocity is below 100 cm/μs. While the zipper time, $\approx$10 ns, is comparable to the overall pulse width ($\approx$15 ns), the zipper
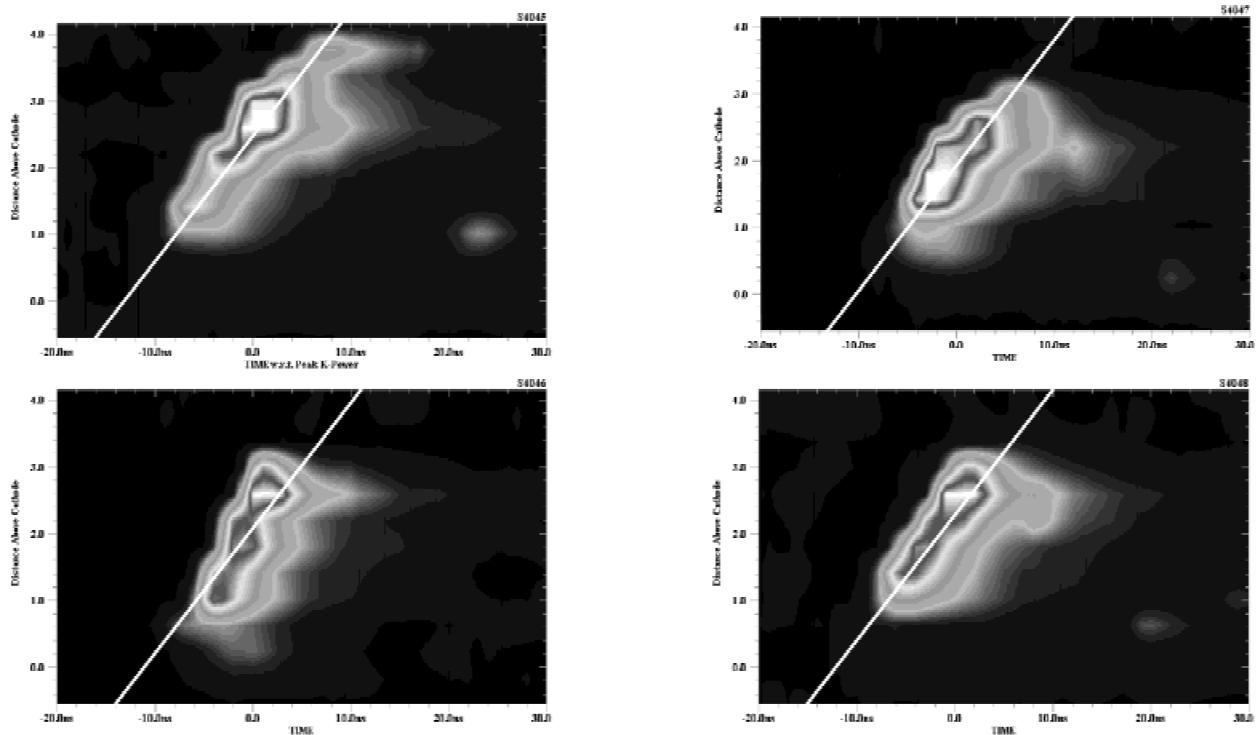
Fig. 40. Zipper images for four consecutive shots, 4045–4048; relatively consistent zipper implies repeatable gas flow, initiation, and implosion dynamics.

time is not dominant. The net result is that for our loads, zippering is not limiting performance. In practice, for the range of zippering seen in our experiments, there is no clear correlation of *K*-power or yield with changes in zippering. Figure 41 shows examples for significant zipper changes with only modest yield variations.

A second objective for the zipper data was to help understand differences in performance for different load types. Data from Double-EAGLE, Saturn (Sanford *et al.*, 1996*a*) and ACE 4 (Coleman *et al.*, 1997) all show that uniform fill gas loads perform much better than nominal shell gas loads. The qualitative explanation is snowplow stabilization: The constant addition of mass, as the implosion runs into a uniform fill, mitigates the growth of instabilities. The shell's losses due to instabilities far outweigh the ideally greater efficiency of an imploding shell as a converter of generator energy into radiation.

In practice, shell nozzles produce shell flows only near the nozzle. Far from the nozzle, all flows tend to become more nearly uniform fills. Hence one might argue that true shell flows have not been given a chance to perform well, especially if there is significant zippering, that is, if the uniform fill part of the flow implodes well before the shell portion arrives on axis. But in fact, gas flow timing on Double-EAGLE was adjusted on some shots to give low zippering. Figure 42 shows three examples with zippering no larger than for the uniform-fill loads; compare with Figure 41. Yet in all cases, the radiated *K*-power is more than a

factor of 2 lower for the shell-like flow near the nozzle. It was always the more filled-in flow away from the nozzle that radiates best.

7.2.3. Quantitative interpretation of zipper timing

Initial conditions in the *z*-pinch can affect the radiation output. Within the last few years, Sandia National Laboratories has demonstrated much higher radiated power as the interwire gap in wire arrays is decreased (Deeney *et al.*, 1998*b*; Sanford *et al.*, 1996*b*). Experiments and models are beginning to offer an explanation for this result. In particular, it is not sufficient that the wire array loads define the initial location of the cold mass. How the individual wires initially expand, the size and timing of the prepulse, and the surface conditions of the wires play significant roles. The better-than-expected performance of long-implosion-time wire arrays at Sandia (*vs.* smaller diameter arrays) may be explained as follows. The time scale for merging of the perturbations in individual wires is fixed by the interwire gap and the properties of the wire material; the longer implosion time allows that merging to occur before significant radial inward acceleration occurs.

For the gas puff loads, one might hope that there are comparable details of the initial conditions that, if controlled, would translate into better performance *via* an understanding of the implosion process. The demonstration of consistent zippering in Figure 40 implies some consistency of initial conditions but not true control.
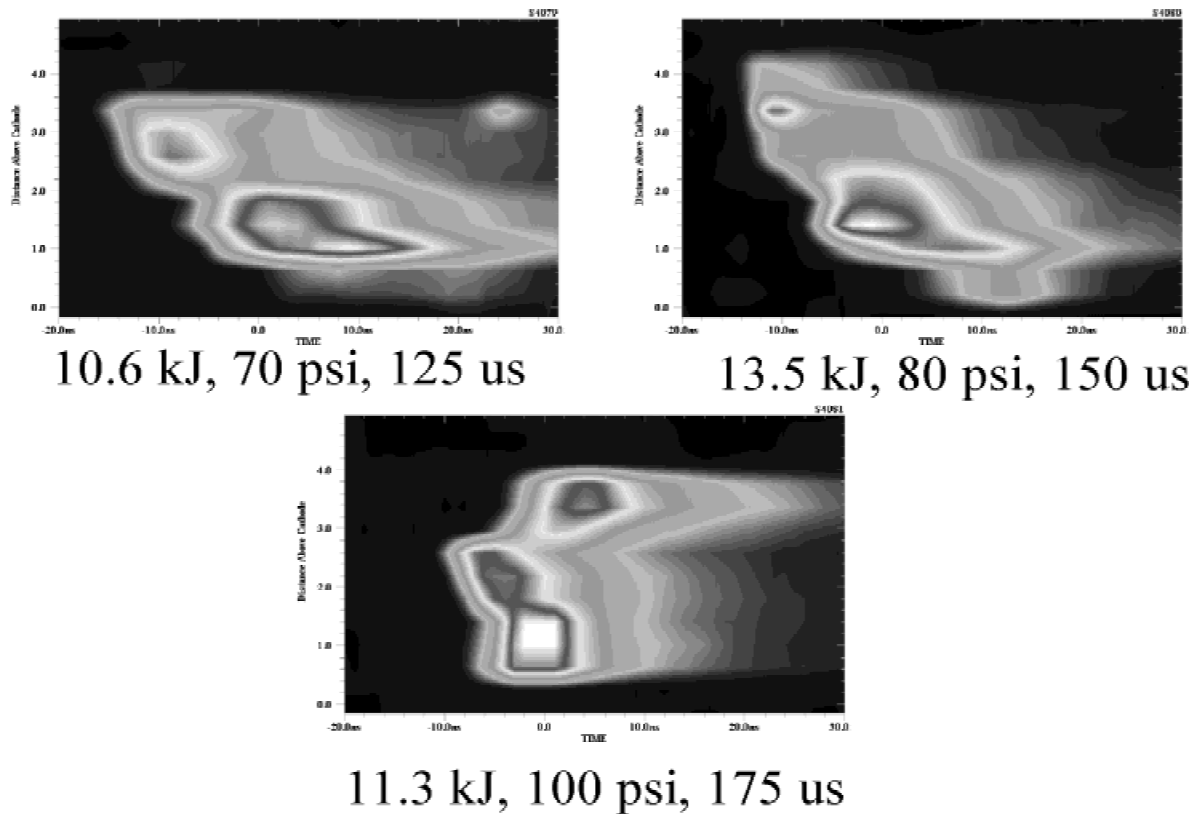
Fig. 41. Modest variations in zippering for 7-cm uniform-fill loads do not give large variations in radiation output: shots 4079–4081. Gas pressures and flow times are listed.

Now, however, we have neutral gas interferometry data that establish where the cold gas is at the beginning and how reproducible the flow is. Do we have any reason to believe that details of the gas flow really matter that much? The best way to address that question would be to use the measured gas flows in 2-D MHD calculations coupled to detailed radiation models.

But to begin, we have used the gas flow data from NRL (Weber *et al.*, 1997) in simple 1-D snowplow calculations. The measured load currents were used to drive the calculations. Implicitly, this approach ignores mass flows in the axial (z) direction and it ignores losses due to instabilities. For both the 5-cm-diameter shell nozzle and the 7-cm-diameter solid-fill, we looked at cases with low gas-flow time and a larger flow time. Per the gas-flow data, the relative variation in imploding mass (*vs.* axial distance) is large for low flow times. Because the implosion time increases monotonically with mass/length, we would expect zippering to be larger with low flow time, when the anode-to-cathode mass difference is greatest.

The first zippering example, Figure 43, is for a 7-cm nozzle shot with long flow time, shot #4081. The heavy black line is the predicted implosion time based on the gas density data at 2-mm, 2-cm, and 4-cm elevations. The actual zipper data show virtually no zipper. The prediction for implosion times of the simple model is remarkably

good although about 10-ns early at the anode side of the AK gap.

The second example, Figure 44, is for a 7-cm nozzle shot with short flow time, shot #4079. As expected from the axial mass gradient data, there was more zippering in the shot. The prediction for implosion time also predicts systematic zippering. The qualitative character of the observed zippering is reproduced by the calculation.

A third example, Figure 45, is for a 5-cm-diameter shell nozzle shot with long flow time, shot #4073. The data show low zippering as expected, although *K*-shell power near the nozzle (cathode) end is low. The model does a good job of predicting arrival time, especially far from the cathode where the flow is more nearly a uniform fill.

Last, a fourth example, Figure 46, is for the 5-cm shell with low flow time, shot #4068. The data show high zipper as expected with very weak *K*-shell power near the cathode end. Again, the model does a good job of predicting arrival time, especially far from the cathode where the flow is more nearly a uniform fill. Even near the cathode, the model is consistent with the low level, late emission seen in the zipper data.

These examples show that we have some basic understanding of the initial conditions, initiation, and implosion of the gas loads. We can model the gas puff implosion times with an accuracy that is the equal of wire loads. Next, 2-D
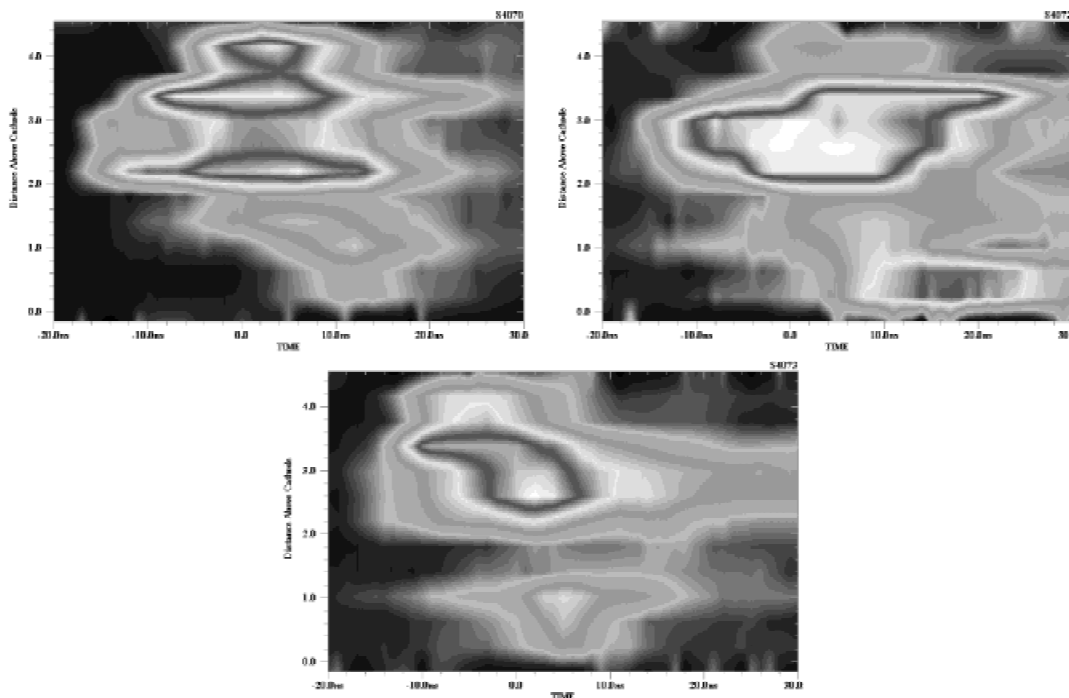
Fig. 42. Zipper images for three shots (4070, 4072, and 4073) using the 5-cm shell.

MHD models should be used to see if we can predict the variation of radiated power with axial position.

7.2.3. Zipper data for wire loads

In principle, the zipper effect (the systematic variation of implosion time with distance across the AK gap) is due to a systematic variation in mass loading (mass per unit length) and radial extent across the AK gap. But for wire loads, there is no mass gradient, so there should be no zipper. However,

as Figure 47 shows, while wire loads show no systematic zipper, they do show significant power variations along their length. Even modestly high wire count arrays, which have shorter pulse widths and higher powers, have more than a factor of 2 variations in K-shell power density (watts per centimeter) along their length. It is likely that these variations are due to instability growth that produces bubble and spike structures. The dominant wavelength of the structures is roughly 5 mm, although shorter wavelengths
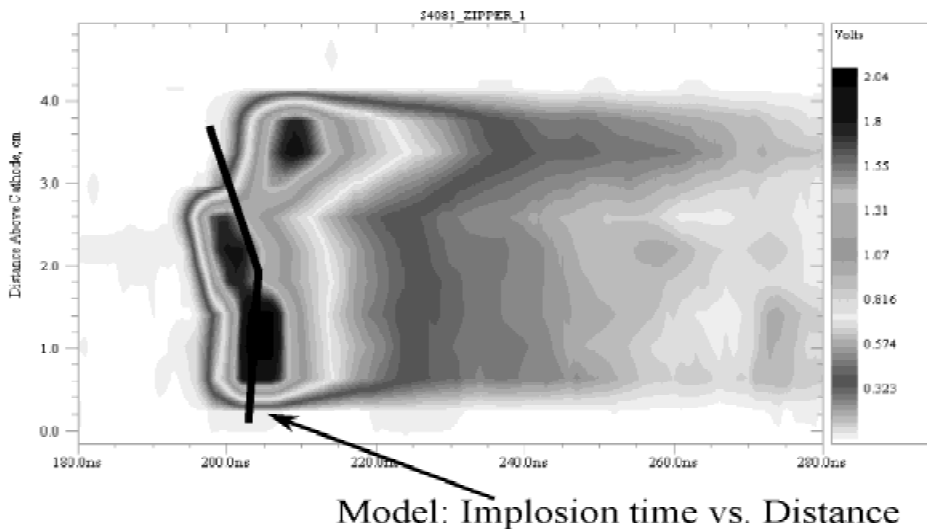

Fig. 43. Comparison of zipper data and simple model of implosion time for 7-cm shot 4081, 175-μs flow time, 100-psia plenum pressure.
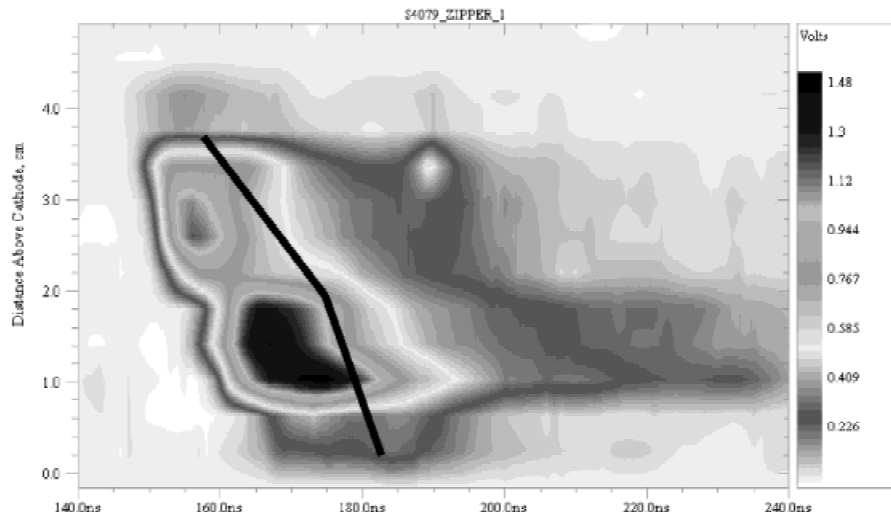
Fig. 44. Comparison of zipper data and simple model of implosion time for 7-cm shot 4079, 125-μs flow time, 70-psia plenum pressure.

might be missed given the 3-mm spatial resolution of the zipper array.

7.2.4. Summary of load features seen with the zipper array

For short- (100 ns) and long- (200 ns) pulse aluminum wire arrays, there is no systematic zipper. But large ($>2\times$) variations in K-shell power are still present on a length scale of ~ 0.5 cm. Increased wire counts improve peak power but do not eliminate axial variations in the power.

In contrast, the gas puff loads do show a systematic zipper. However, it is not large enough in most cases to upset the performance of the pinch. For both short-pulse and long-pulse shell flows, the truly annular flow near the nozzle is seen to radiate poorly. The more filled-in flow far from the nozzle radiates best. The solid-fill flows also tend to radiate more uniformly along their entire length. Gas flow timing and plenum pressure can be adjusted to significantly change the zippering behavior.

There is growing evidence that we can be quantitative in our understanding of gas puff loads. Gas density measurements can be coupled with the measured current drive to predict the observed implosion time of a load as a function of position across the AK gap. This implies reproducible and plausible behavior for the gas flow, current initiation, and implosion dynamics of these loads. Finally, the zipper data show that even good pinches show significant variations with axial distance. Hence simple comparisons of global data (K-shell power waveforms, a pinch diameter, a single
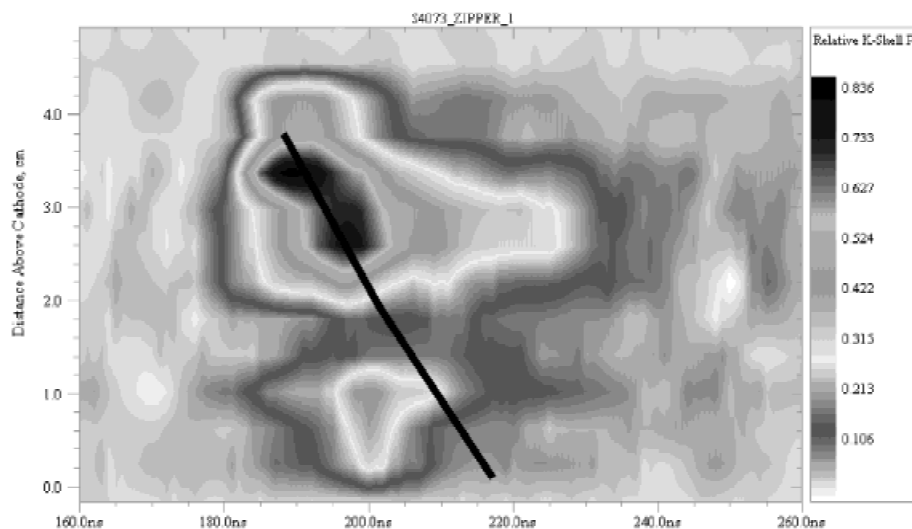

Fig. 45. Comparison of zipper data and simple model of implosion time for 5-cm shot 4073, 235-μs flow time, 22-psia plenum pressure.
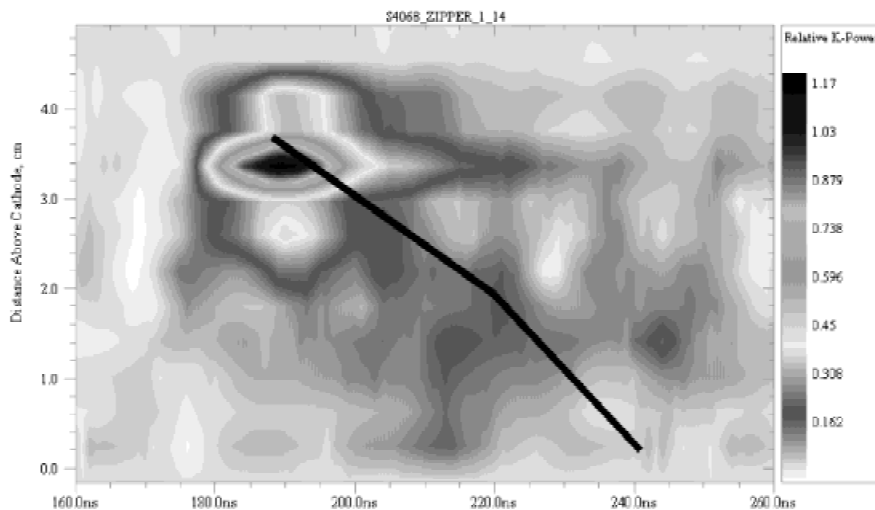
Fig. 46. Comparison of zipper data and simple model of implosion time for 5-cm shot 4068, 135-μs flow time, 60-psia plenum pressure.

temperature, etc.) with 0-D, 1-D models should proceed with caution.

7.3. Use of CCDs for X-ray imaging on *z* pinches

Several key *z*-pinch diagnostics produce 1-D and 2-D images: spatially resolved spectrographs and pinhole cameras.

These diagnostics routinely use film to record the image. Film is compact and relatively inexpensive for qualitative use. But it has high facility costs (dark room and micro-densitometer upkeep), and "hidden" expenses (film and processing-chemicals acquisition plus hazardous-waste disposal). Scientifically, the "costs" are also high. Accurate quantitative information requires operators trained in care-
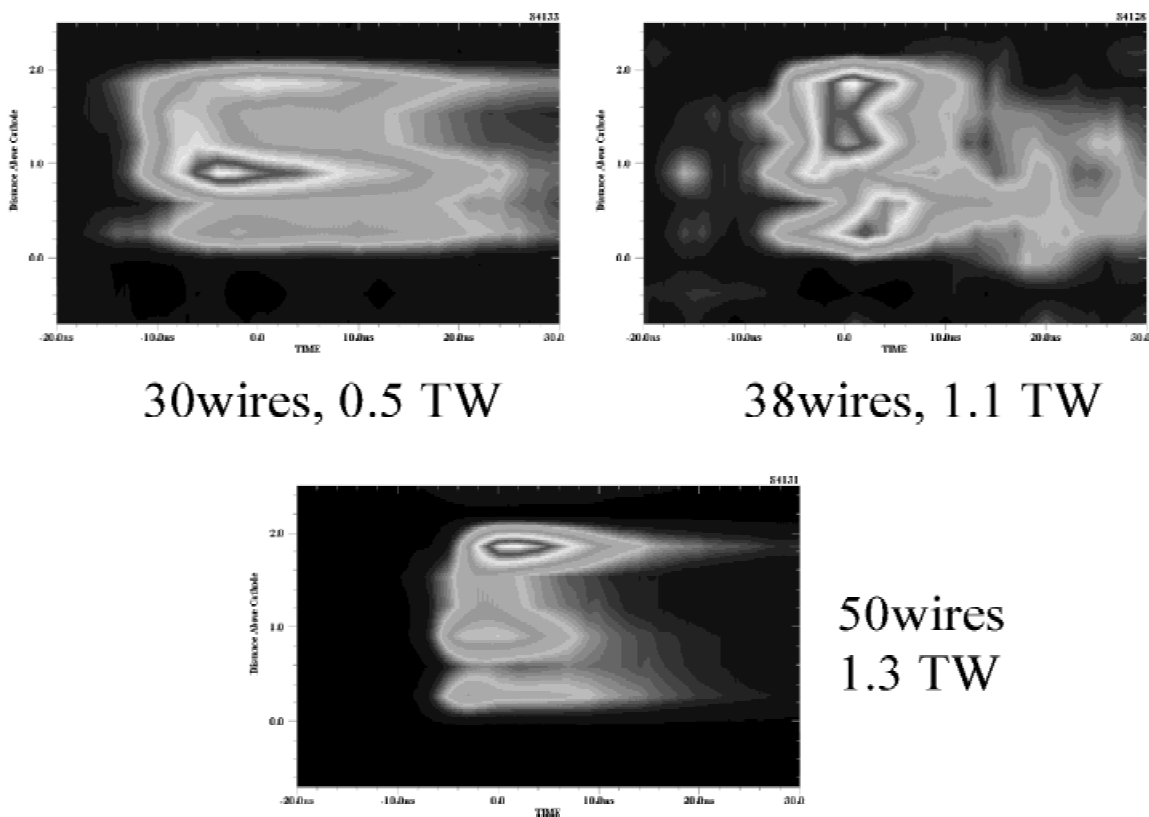

Fig. 47. Zipper data for three long-pulse (214 ns) aluminum shots: #4133 with 30 wires, 0.5 TW peak *K*-shell power; #4128 with 38 wires, 1.1 TW; #4131 with 50 wires, 1.3 TW. Each array used a diameter of 4.0 cm.
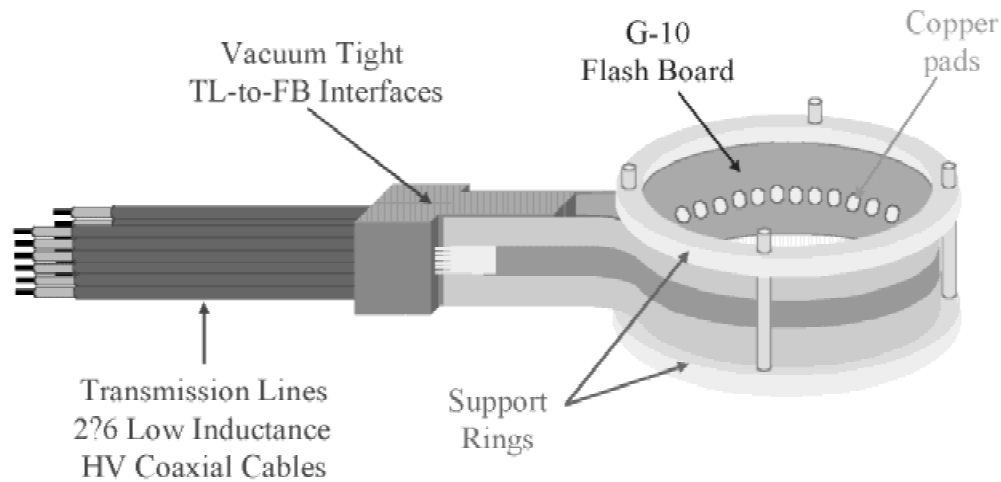
Fig. 48. Schematic of the DE preionizer.

fully controlled film development and digitization, capital investment in expensive (~$100k) equipment, such as a microdensitometer, and significant labor (i.e., time). Typically the developed film is available for qualitative inspection hours after a test. Quantitative data from the image requires hours or days for microdensitometer scanning.

Over the last few years, we have successfully demonstrated the use of charge-coupled devices (CCD) as a replacement for film. With a CCD, the qualitative image can be viewed within seconds of a test. We get quantitative image and spectral data within 30 minutes. This has allowed us to make quick decisions about the configuration of the next shot, thus enabling more effective load development. See Failor *et al.* (2001) for the details.

7.4. UV preionizer

This section describes the development of ultraviolet (UV) preionization sources for use with our long-implosion-time loads. These sources had the specific objective of being very uniform azimuthally. The idea is that instability development during an implosion is seeded in part by the level of nonuniformity in the initial conditions of the pinch. More uniform preionization of the gas should promote more uniform current flow on the gas column, that is, more uniform initiation will reduce the seed for the instability.

In the past, usual practice was to place a localized source of UV light, a small flashboard, to one side of the gas puff. However, since neutral argon at the typical densities used is rather opaque in the UV, there is some question about the uniformity of the ionization. Hence we designed a cylindrically symmetric preionizer. Using the NRL precision interferometer in its two-color mode to distinguish electrons from neutrals, ionization levels >1% were measured at the outer edge of the flow, with penetration consistent with $\geq 100\ \mu J/cm^2/\mu s$ of 16–27 eV radiation. Using the circular preionizer, data from DM2 PRS experiments suggested that

preionization helped to eliminate the low yield shots and reduce shot-to-shot variation.

Flashboard-generated UV light is a suitable source for preionizing gas puffs. The photoionization cross section for neutral argon exhibits a broad maximum in the 16–27 eV range (Verner *et al.*, 1996). Experiments indicate that over 60% of the UV emission from such flashboard sources is in the 10- to 20-eV range with the remainder emitted mainly between 20 and 70 eV (Woodworth & McKay, 1985). Thus, there exists a good match between the flashboard emission spectrum and the absorption properties of argon.

To generate an azimuthally symmetric ionization source, two semicircular flashboards are used. A dedicated pulser drives each flashboard with a peak current of 60 kA in a 1.3-μs pulse. The preionizer is represented schematically in Figure 48.

The flashboards are made of thin (0.254 mm), imprinted G-10 fiberglass boards that are robust and long lasting. During the PRS experiments on Double-EAGLE, each pair of flashboards usually lasted more than 10 shots before replacement. Due to time and cost constraints, no systematic comparison shots have been made to test the effectiveness of the preionization to increase *K*-shell yield at the ~4 MA level.

ACKNOWLEDGMENT

REFERENCES

APRUZESE, J. *et al.* (1997). *J. Quant. Spectros. Rad-Tranf.* **57**, 41.
APRUZESE, J.P. *et al.* (1998). *Phys. Plasmas* **5**, 4476.
BAKSHT, R.B. *et al.* (1998). *IEEE Trans. Plasma Science* **26**, 1259.
BLOOMQUIST, D.D. *et al.* (1987). *Proc. of the 6th IEEE Pulsed Power Conf.*, 310.
BOOK, D.L. (1996). *Phys. Plasmas* **3**, 354.
CHAPMAN, M. (1980). S-Cubed Report No. SSS-R-80-4620.

COLEMAN, P.L. *et al.* (1997). *Fourth Int. Conf. on Dense Z Pinches*, AIP Proceedings #409, p. 119.

DEENEY, C. *et al.* (1994). *J. Appl. Phys.* **75**, 2781.

DEENEY, C. *et al.* (1995). *Phys. Rev. E.* **51**, 4823.

DEENEY, C. *et al.* (1998*a*). *Phys. Rev. Lett.* **81**, 4883.

DEENEY, C. *et al.* (1998*b*). *Phys. Plasmas* **5**, 2431.

FAILOR, B.H. *et al.* (2001). *Rev. Sci. Instrum.* **72**, 1232.

FRAZIER, G.B. *et al.* (1983). Digest of Technical Papers*, 4th IEEE Pulsed Power Conf.*, 583.

GLENZER, S.H. *et al.* (1997). *Phys. Rev.* E **55**, 927.

GOLBERG, S.M. & VELIKOVICH, A.L. (1993). *Phys. Fluids B* **5**, 1164.

HAMMER, J.H. *et al.* (1996). *Phys. Plasma* **3**, 2063.

MOSHER, D. *et al.* (1998). *IEEE Trans. Plasma Sci.* **26**, 3.

PEREIRA, N.R. & DAVIS, J. (1988). *J. Appl. Phys.* **64**, R1.

PETERSEN, D. *et al.* (1996). *Phys. Plasmas* **3**, 368.

PETERSEN, D. *et al.* (1997). *AIP Conf. Proc.* **409**, 201.

PRICE, D. *et al.* (1999). *Proc. of the 12th IEEE Pulsed Power Conf.*, 489.

RIORDAN, J.C. *et al.* (1998). *Bull. Am. Phys. Soc.* **43**, 1905.

RIX, W. *et al.* (1993). *Proc. of the 9th IEEE Pulsed Power Conf.*, 115.

RODERICK, N. *et al.* (1998). *Phys. Plasmas* **5**, 1477.

SANFORD, T.W.L. *et al.* (1996*a*). Digest of Technical Papers, *23rd IEEE Int. Conf. on Plasma Sci.*, 251.

SANFORD, T.W.L. *et al.* (1996*b*). *Phys. Rev. Lett.* **77**, 5063.

SINCERNY, P. *et al.* (1995). *Proc. of the 10th IEEE Pulsed Power Conf.*, 405.

SONG, Y. *et al.* (2000). *Rev. Sci. Instrum.* **71**, 3080.

SPIELMAN, R.B. *et al.* (1989). *AIP Conf. Proc.* **195**, 3.

SPIELMAN, R.B. *et al.* (1998). *Phys. Plasmas* **5**, 2105.

SZE, H. *et al.* (2000). *Phys. Plasmas* **7**, 4223.

SZE, H. *et al.* (2001). *Phys. Plasmas* **8**, 3135.

STEPHANAKIS, S.J. *et al.* (1998). Naval Research Laboratory Pulsed Power Technote No. 98-05.

THORNHILL, J.W. *et al.* (1996). *J. Appl. Phys.* **80**, 710.

VELIKOVICH, A.L. *et al.* (1996). *Phys. Rev. Lett.* **77**, 853.

VERNER, D.A. *et al.* (1996). *Astrophys. J.* **465**, 487.

WEBER, B. *et al.* (1997). Naval Research Laboratory Pulsed Power Physics Technotes No. 97-08.

WHITNEY, K.G. *et al.* (1990). *J. Appl. Phys.* **67**, 1725.

WHITNEY, K.G. *et al.* (1994). *Phys. Rev. E.* **50**, 2166.

WONG, K.L. *et al.* (1998). *Phys. Rev. Lett.* **80**, 2334.

WOODWORTH, J.R. & MCKAY, P.F. (1985). *J. Appl. Phys.* **58**, 3364.